AGU PUBLICATIONS

JGR

Journal of Geophysical Research: Atmospheres

RESEARCH ARTICLE

10.1002/2016JD025798

Special Section:
Studies of Emissions and Atmospheric Composition, Clouds and Climate Coupling by Regional Surveys, 2013 (SEAC4RS)

Key Points:
- The first seasonal study of aerosol particle vertical distribution over the Southeast U.S. was conducted during SEAC^{4}RS using an HSRL lidar
- Particles mapped well to key boundary layer levels, with free tropospheric particles being largely sequestered under the melting level
- Occasional but strong injections of smoke up to the tropopause were observed associated with smoke ingested into mesoscale convective system

Correspondence to:
J. S. Reid,
jeffrey.reid@nrlmry.navy.mil

Citation:
Reid, J. S., et al. (2017), Ground-based High Spectral Resolution Lidar observation of aerosol vertical distribution in the summertime Southeast United States, *J. Geophys. Res. Atmos.*, *122*, 2970–3004, doi:10.1002/2016JD025798.

Received 18 AUG 2016
Accepted 20 JAN 2017
Accepted article online 26 JAN 2017
Published online 9 MAR 2017

Ground-based High Spectral Resolution Lidar observation of aerosol vertical distribution in the summertime Southeast United States

Jeffrey S. Reid[1], Ralph E. Kuehn[2], Robert E. Holz[2], Edwin W. Eloranta[2], Kathleen C. Kaku[3], Shi Kuang[4], Michael J. Newchurch[5], Anne M. Thompson[6], Charles R. Trepte[7], Jianglong Zhang[8], Samuel A. Atwood[9], Jenny L. Hand[10], Brent N. Holben[6], Patrick Minnis[7], and Derek J. Posselt[11]

[1]U.S. Naval Research Laboratory, Monterey, California, USA, [2]Space Sciences Engineering Center, University of Wisconsin-Madison, Madison, Wisconsin, USA, [3]CSRA, Monterey, California, USA, [4]Earth System Science Center, University of Alabama, Huntsville, Alabama, USA, [5]Department of Atmospheric Science, University of Alabama, Huntsville, Alabama, USA, [6]NASA Goddard Space Flight Center, Greenbelt, Maryland, USA, [7]NASA Langley Research Center, Langley, Virginia, USA, [8]Department of Atmospheric Sciences, University of North Dakota, Grand Forks, North Dakota, USA, [9]Department of Atmospheric Science, Colorado State University, Fort Collins, Colorado, USA, [10]CIRA, Colorado State University, Fort Collins, Colorado, USA, [11]Jet Propulsion Laboratory, California Institute of Technology, Pasadena, California, USA

Abstract As part of the Southeast United States-based Studies of Emissions and Atmospheric Composition, Clouds and Climate Coupling by Regional Surveys (SEAC^{4}RS), and collinear with part of the Southeast Atmosphere Study, the University of Wisconsin High Spectral Resolution Lidar system was deployed to the University of Alabama from 19 June to 4 November 2013. With a collocated Aerosol Robotic Network (AERONET) sun photometer, a nearby Chemical Speciation Network ($PM_{2.5}$) measurement station, and near daily ozonesonde releases for the August–September SEAC^{4}RS campaign, the site allowed the region's first comprehensive diurnal monitoring of aerosol particle vertical structure. A 532 nm lidar ratio of 55 sr provided good closure between aerosol backscatter and AERONET (aerosol optical thickness, AOT). A principle component analysis was performed to identify key modes of variability in aerosol backscatter. "Fair weather" days exhibited classic planetary boundary layer structure of a mixed layer accounting for ~50% of AOT and an entrainment zone providing another 25%. An additional 5–15% of variance is gained from the lower free troposphere from either convective detrainment or frequent intrusions of western United States biomass burning smoke. Generally, aerosol particles were contained below the 0°C level, a common level of stability in convective regimes. However, occasional strong injections of smoke to the upper troposphere were also observed, accounting for the remaining 10–15% variability in AOT. Examples of these common modes of variability in frontal and convective regimes are presented, demonstrating why AOT often has only a weak relationship to surface $PM_{2.5}$ concentration.

1. Introduction

The National Aeronautics and Space Administration (NASA) Studies of Emissions and Atmospheric Composition, Clouds and Climate Coupling by Regional Surveys (SEAC^{4}RS) [*Toon et al.*, 2016] was a mission to compressively examine the multifaceted North American convection, air chemistry, and radiation environments. Conducted in August and September 2013, the SEAC^{4}RS mission performed operations over much of North America, from the Gulf of Mexico to Canada, and the Pacific Ocean to the Carolinas. True to its name, the SEAC^{4}RS mission design was multidisciplinary, combining aerosol, chemistry, convection, and radiation elements to support NASA objectives on climate research and monitoring the atmosphere from space. Three aircraft were deployed (the NASA DC-8 and ER2 and the SPEC LearJet), ground sites were established, and modeling simulations were conducted for a mission timed to observe the peak and subsequent decrease of Southeast United States (SEUS) haze and convection season and coincide with wild and agricultural biomass burning emissions. The SEAC^{4}RS deployment complimented the National Science Foundation and National Oceanic and Atmospheric Association (NOAA) June–July Southeast Atmospheric Study (SAS) deployments with its own P-3 aircraft and ground site designed to study the development of SEUS haze. Between these missions, the aerosol environment of the SEUS was examined in unprecedented detail.

As part of SEAC^{4}RS, a ground network was deployed across the SEUS to provide context to research flights [*Toon et al*., 2016]. Components included a synoptic Aerosol Robotic Network (AERONET) [*Holben et al*., 1998] of sun photometer and Southeast American Consortium for Intensive Ozonesonde Network Study (SEACIONS) ozonesonde sites [*Toon et al*., 2016]. The ground network included the 18 June to 4 November 2013 deployment of the University of Wisconsin (UW) Space Sciences and Engineering Center (SSEC) 532 nm High Spectral Resolution Lidar (HSRL) to the University of Alabama Huntsville (UAH) National Space Sciences Technology Center (NSSTC) Regional Atmospheric Profiling Center for Discovery (RAPCD) lidar facility. Sponsored by the NASA Cloud-Aerosol Lidar and Infrared Pathfinder Satellite Observations (CALIPSO) science team as a contribution to SEAC^{4}RS, the UW HSRL provided the first ever direct measurements of diurnal aerosol particle and cloud backscatter coefficients in the SEUS. Such information is critical in understanding aerosol behavior and making progress regarding the observability of surface air quality, cloud condensation nuclei, and aerosol radiative effects. Such data are also useful regarding our understanding of aerosol and cloud particle size and optical properties.

Many of the SEAC^{4}RS objectives have strong dependencies on the vertical dimension of aerosol properties. Certainly, for "North American polluted environments," scientists have long reported on the overall nature of aerosol layering in the boundary layer and lower free troposphere [e.g., *Uthe*, 1972; *Kunkel et al*., 1977; *Cohn and Angevine*, 2000; *Clarke et al*., 2007; *Shinozuka et al*., 2007; *Thornhill et al*., 2008; *Su et al*., 2008; *Berg et al*., 2009; *Kassianov et al*., 2010; *Chu et al*., 2015]. Progress from demonstration cases to systematic observation and prediction requires an in-depth understanding of the processes of the aerosol system and, in particular, an establishment of what the free parameter space in the environment truly is. Accurate characterization of diurnal variability in aerosol vertical distribution is critical in relating remote sensing signals to aerosol properties and lifecycles [e.g., *Fochesatto et al*., 2001; *Henne et al*., 2004; *Guiot et al*., 2006; *Chou et al*., 2007; *Pal et al*., 2014; *Toth et al*., 2014]. Attention should also be paid to cleaner conditions when aerosol-cloud sensitivities are largest and aerosol measurement signal-to-noise is lowest. In these regards, measurement of the diurnal vertical distribution of aerosol particles in the SEUS has been elusive. While CALIPSO has been providing day and night vertical profiles, the data are spatially sparse due to its 22° orbit, and profiles are also relatively noisy in the mixed layer. Poor signal-to-noise for deep but low concentration extinction layers is also problematic, even if overall layer aerosol optical depth (AOD) is moderately high. Airborne HSRL and other in situ measurements, while providing significant improvements and high signal-to-noise, are limited in duration. Other ground-based lidar deployments in the region are not optimized for thin aerosol layers. The UW-HSRL lidar deployed to Huntsville is sensitive to aerosol backscatter and thus provided an opportunity for a summer observation aerosol particle vertical profiles.

The primary purpose of this paper is to provide an overview of the summertime 2013 UW-HSRL deployment to Huntsville and offer the necessary context to a number of other ongoing efforts to explore the aerosol and cloud environment during the SEAC^{4}RS and SAS missions. Notably, through the demonstration of the dominate modes of variability in aerosol vertical distribution this effort provides phenomenological context for challenging aerosol applications such as regional air quality, aerosol layering processes, cirrus clouds, and ultimately model assimilation. Here we give an introductory overview of the deployment including a thorough description of the UW-HSRL and other available data sets collocated at the site in section 2. Included is a discussion of derived HSRL parameters and the natural variability of the vertical profile as provided by an objective principal component analysis (PCA). This is followed by findings regarding regional variability in aerosol vertical distribution over the study period in section 3. An example of a canonical "fair weather day" is used to denote recurring aerosol vertical features followed by a deployment time series that illustrates day-to-day variability. Three additional canonical examples of important aerosol environments are provided with their own discussion showing the complexity of aerosol particle vertical distribution in section 4: (1) a polluted summertime convective environment, (2) the passage of an early autumn frontal feature, and (3) the most significant biomass burning event to be transported over the site. We finally close with a summary and outline ongoing efforts to further exploit this data set in section 5.

2. Methods

Significant amounts of data complemented the UW-HSRL deployed to the UAH RAPCD lidar facility, from 19 June to 4 November 2013. In context, the core SEAC^{4}RS mission airborne operations period out of Houston TX

occurred 9 August through 23 September 2013 [*Toon et al*., 2016]. The UW-HSRL deployment also coincided with a portion of the NOAA WP-3D airborne operations for SAS [e.g., *Wagner et al*., 2015] conducted in June and July 2013. In the following subsections, specifics of the UW-HSRL system and a description of the Huntsville site and other ancillary remote sensing and modeling data are provided. In the section's final subsection, we describe the baseline performance of the UW-HSRL system and the natural modes of variability in vertical distribution of aerosol backscatter.

2.1. UW HSRL Lidar System

HSRL systems generate calibrated measurements of aerosol or cloud particle backscatter cross section. For environments of sufficient signal-to-noise, volumetric light extinction coefficients can be derived. As outlined in *Shipley et al*. [1983], *Eloranta* [2005], and *Hair et al*. [2008], this is done by the HSRL's technology of separately measuring the Cabannes-Brillioun scattering (molecular scattering without the rotational Raman component normally included in the Rayleigh cross section) and total scattering (particle + all molecular). In short, this is accomplished by exploiting the fact that the molecular backscatter is wavelength broadened due to Doppler shifts in rapidly moving/rotating molecules, whereas particle scattering does not have such a pronounced effect. By means of a measurement of total return and total return minus the exact emitting wavelength through the use of a narrow notch filter, one can isolate molecular backscatter from total backscatter. Using Rayleigh scattering theory and an atmospheric temperature and density profile, the measured molecular signal provides a known target at each altitude from which the particulate backscatter cross section can be determined. If sufficient signal exists, particulate extinction cross section is provided by calculating the slope of the measured molecular return, corrected for the molecular attenuation [*Eloranta*, 2005]. The lidar ratio (S_a), or extinction-to-backscatter ratio, can also then be derived if sufficient signal-to-noise exists (See section 2.4 for a more thorough discussion.). The lidar ratio is related to the size, composition, and habit of the aerosol and cloud particles. Additionally, the HSRL measures the aerosol/cloud depolarization ratio, with values greater than 25% (mean ~40%) are indicative of ice clouds or dust [e.g., *Liu et al*., 2004]. Low values indicating spherical particles and intermediate values (i.e., ~10%) indicating a mix of spherical and nonspherical particles or sometimes indicating nonspherical cores within biomass burning smoke particles [e.g., *Burton et al*., 2012].

The UW HSRL system deployed for the SEAC^{4}RS campaign to the UAH RAPCD facility at Huntsville, AL, was hardened for continuous use. The transmitting laser was a diode pumped, intracavity, frequency doubled Nd-YAG lase at 532 nm, with 200 mW average power, and a pulse repetition rate of 4 kHz. The laser beam was transmitted through a 40 cm receiving afocal telescope in a transceiver configuration (that is, the same telescope manages emission and receiving). This arrangement simplifies the task of aligning the transmitted beam and the receiver field of view (FOV) and allows the system to operate with a 100 μrad (full angle) FOV, improving signal-to-noise. A second 2.5 cm diameter/1 mrad FOV telescope sat behind the secondary mirror fiber coupled to a third iodine absorption channel providing a wide (WFOV) molecular channel. In this configuration, the receiver detectors consisted of three iodine absorption channels, aka "molecular" channels, one combined or "total scattering" channel and one cross-polarized channel. The molecular channel with the 1 mrad WFOV was used to correct for the system geometric factor. The geometric factor arises from the receiver being out of focus for ranges less then ~4 km. For precise extinction measurements below 4 km the WFOV channel allows for periodic calibration of the geometric factor without requiring clear-sky conditions. For 532 nm depolarization, outgoing laser pulse is linearly polarized. A polarizing beam splitter in the receiver was used to separate the parallel and perpendicular returned signals in the combined channel with each polarization having its own detector. The relative gain and cross talk of the two channels was measured off-line and has proven to be stable.

The UW HSRL operated near continuously from 19 June to 3 November 2013, with notable outages from 20 to 22 August and 13 to 17 September. The system provided aerosol backscatter and depolarization every 1 min at 30 m resolution. Figures in this paper of aerosol backscatter draw from this data set. For quantitative analysis in this overview paper, data were aggregated to 90 m vertical and 15 min except where noted (for spatial and temporal aggregation, separate retrievals are required). Due to uncertainties near the lidar aperture, data in the very near field (<200 m) were not used in the analysis but rather assumed constant below the 200 above ground level (agl) level when column integration was necessary. Clouds were flagged via a backscatter cross-section threshold algorithm, where empirical thresholds were determined from backscatter and

depolarization statistics for the entire field campaign and via expert inspection of lidar images. Also generated for this data set was a mixed layer height product based on *Piironen and Eloranta* [1995]. This method is based on the assumption that the first observed significant peak in aerosol backscatter corresponds to the maximum in relative humidity at the top of a well-behaved mixed layer.

All UW HSRL observations used in this paper are available through the HSRL web interface (http://hsrl.ssec.wisc.edu/). Quick look imagery is pregenerated allowing efficient browsing of selected days; however, the system is designed to provide on demand processing of the HSRL data. This approach allows users to customize the temporal and vertical averaging to optimize the data for a given application. Given the complexity of the system, it is imperative that the data quality and calibration be carefully assessed before using the products for quantitative analysis. The SEAC^{4}RS measurements used in this manuscript have been calibrated and inspected by the UW-HSRL group. It is recommended that a user contact the HSRL team before using the HSRL for science applications to insure the integrity of the data quality provided by the web interface.

2.2. Overview of the Ground Huntsville Site

The NSSTC/RAPCD facility at Huntsville, AL (34.725°N; 86.645°W), was a key ground site for the SEAC^{4}RS campaign. With its existing lidar facilities and knowledgeable staff, it was a logical location to place the UW-HSRL for the SEAC^{4}RS mission. Further, the facility and nearby region hosted a number of other useful instrumentation to support the analysis of the UW-HSRL data. RAPDC is home to a facility for the monitoring of air pollution by remote sensing. Included in the combined NSSTC/RAPCD package was a differential absorption lidar (DIAL) for ozone monitoring [*Kuang et al.*, 2011], Fourier transform infrared spectrometers, ceilometers, weather stations, radiometers, and AERONET sun photometer. Also, during the SEAC^{4}RS mission airborne period, near daily ozonesondes were released as part of the participating Southeast American Consortium for Intensive Ozonesonde Network Study (SEACIONS) effort (http://croc.gsfc.nasa.gov/seacions/).

The RAPCD facility is located at the NSSTTC building on the western side of the city of Huntsville with an elevation of ~220 m. Given building height, the lidar transmitter was at 230 m above mean sea level (msl). Overall the local terrain is flat, with the exception of a line of hills 10–15 km to the east and southeast of the site, protruding at an additional elevation of 200–350 m. The closest topographic feature is an additional 200 m hill 5 km to the southeast. Relative to the rest of the terrain (northeast through southeast), no other feature more than 100 m exists for over 100 km. To evaluate aerosol source regions over the Huntsville site, air mass histories for selected aerosol layers were generated using the NOAA Hybrid Single-Particle Lagrangian Integrated Trajectory (HYSPLIT) Version 4.9 Model [*Draxler and Hess*, 1997, 1998; *Draxler*, 2004] based on the Global Data Assimilation System-1, 1°×1° global meteorological data set [*Kleist et al.*, 2009]. Back trajectories were run back 72 h.

Several instruments are core to this analysis. Lidar data were analyzed in conjunction with AERONET sun photometer data [*Holben et al.*, 1998]. Such data are used to evaluate the HSRL data, to help constrain lidar ratios, and to provide context to what an accurate remote sensing retrieval of aerosol optical thickness (AOT) would be. The UAH sun photometer provided AOT at eight wavelengths (340, 380, 440, 500, 675, 870, 1020, and 1640 nm) plus a 940 nm water vapor channel. In nearly all cases AERONET quality controlled, postcalibrated and internally cloud screened level 2 data were used [*Smirnov et al.*, 2000]. The Spectral Deconvolution Method (SDA) plus [*O'Neill et al.*, 2003; *Kaku et al.*, 2014] was then applied to this level 2 spectral AOT data to extract total, fine, and coarse mode AOT at the 532 nm wavelength that the HSRL lidar operates. An advantage of the SDA plus method is its ability to help screen for cirrus contamination [*Chew et al.*, 2011]. For one case of aerosol particles in a polluted convective environment (section 4.1) level 2 data were unavailable due to the presence of thin cirrus. In this case we applied the SDA plus algorithm to level 1 data with postcalibration but no internal cloud clearing to extract fine mode AOT from the cirrus contamination.

A second key piece of analysis data is from radiosondes. Huntsville is located 140–200 km from a number of operational radiosonde sites. The closest operational radiosonde site was Birmingham, AL, (33.16°N; 86.76°W), ~140 km to the south. While Birmingham released twice daily, the 0/12 Z release schedule corresponded to 7 P.M./A.M. local time outside of core daytime boundary layer conditions. However, we expect that 7 P.M. CDT soundings should be largely similar to late afternoon conditions. Further, this site adequately captured the gross synoptic features, such as the tropopause height and overall tropospheric temperature and humidity structures.

Supplementing the operational radiosonde data were the SEACIONS ozonesondes released during the SEAC^{4}RS campaign. Forty sondes were released between 6 August and 21 September 2013, at 18:00–19:00 Z/13:00–14:00 CDT to coincide with early afternoon boundary layer conditions, midflight airborne activity, and the NASA A-train overpass. The ozonesonde instrument type used is the Droplet Measurement Technologies electrochemical concentration cell, the same instrument as previously supplied by the ENSCI Corporation and used at Huntsville since soundings began there in 1999 [*Newchurch et al*., 2003; *Thompson et al*., 2007]. The ozonesonde uses a 0.5% buffered potassium-iodine solution that has given the best performance when ENSCI-type sondes are evaluated in test chamber and field experiments [*Deshler et al*., 2008; *Smit et al*., 2007]. The ozonesonde measures ozone with a vertical resolution of ~100 m, accuracy better than ±10% and precision better than ±5% throughout the troposphere [*Smit et al*., 2007]. The radiosonde used is the IMet-1 (Intermet Company, Grand Rapids). Pressure offsets between the pressure sensors on the radiosonde were not in agreement with the GPS reading of the IMet-1 and a correction was made, as described in *Stauffer et al*. [2014]. The pressure corrections on ozonesonde readings in the troposphere are small ($<$1%).

During the HSRL deployment the RAPCD ozone DIAL lidar was also periodically run. A calendar of run times is provided online at http://nsstc.uah.edu/atmchem/lidar/DIAL_data.html, last accessed on 1 November 2016. During the working period discussed in this paper, the ozone DIAL measured ozone from 0.1 km up to ~12 km during nighttime and up to ~5 km during daytime with a temporal resolution of 2 min. The vertical resolutions of the DIAL retrievals vary from 150 m near the surface to 750 m at the upper troposphere accommodating the quickly decreasing lidar signal-to-noise ratio with altitude. The measurement accuracy is better than 10% in the lower troposphere and better than 20% in the upper troposphere [*Kuang et al*., 2011].

Other ancillary data used in this overview analysis include air quality data provided by the Environmental Protection Agency's Chemical Speciation Network (CSN) site 4 km to the southeast [*Solomon et al*., 2014]. Data from the CSN site include hourly tapered element oscillating microbalance and one-day-in-three 24 h gravimetry. Roughly one dozen filters were submitted for chemical speciation during the SEAC^{4}RS mission.

2.3. Satellite Remote Sensing Contributions

There are a number of satellite data products relevant to the HSRL data set. Although not discussed in detail in the case studies shown here, they are worth noting in the context of this overview paper. MODIS aerosol (MOD/MYD04) [*Levy et al*., 2013] and cloud (MOD/MYD 06) [*Platnick et al*., 2003, 2016] products were operationally generated for the mission. A notable geographic aspect of the Huntsville site is its location relative to the CALIPSO orbit. On an average of four times per month CALIPSO passed within 15 km of the Huntsville lidar site. Eighteen CALIPSO overpasses occurred when the UW HSRL was operating including daytime overpasses on 18 June, 4 and 29 July, 5 and 21 August, 8 and 22 September, and 8 and 24 October as well as nighttime overpasses on 20 June, 6 and 22 July, 7 and 23 August, 8 and 24 September, and 10 and 26 October. Also, notable is a serendipitous set of Terra orbits; Huntsville is observed by Multiangle Imaging Spectroradiometer (MISR) every 7 days in the very center of orbit path 20 and 21 [*Kahn et al*., 2005]. In addition, Huntsville lies just outside of the left- and right-hand border of orbit paths 19 and 22, respectively. While it does not provide direct coverage, MISR data are collected within 10 km of the site, thus providing additional data on the region.

Specifically for the UW-HSRL deployment a Geostationary Operational Environmental Satellite East (GOES 13) cloud product was generated by NASA Langley Research Center. While the HSRL lidar provides a bottom up perspective of cloud structure, geostationary cloud products can provide cloud top information and a spatial context. Cloud properties were derived every 15 or 30 min with 4 km resolution, using the techniques of *Minnis et al*. [2008a, 2008b, 2011]. The GOES 13 visible channel was calibrated against Aqua MODIS channel 1 using the approach of *Minnis et al*. [2002]. Among the parameters provided for each image time are pixel classification (e.g., clear, ice cloud, and water cloud), shortwave albedo, and outgoing longwave radiation, as well as a variety of properties for cloudy pixels, including cloud effective height, top height, optical depth, particle effective size, and ice or liquid water path. From these pixel values, cloud fraction and averages for a given parameter can be computed for any area. Huntsville retrievals are aggregated on a 10 or 20 km radius. The GOES cloud data are available in digital and image formats at http://www-pm.larc.nasa.gov/SEAC4RS (last accessed in November 2016).

From an airborne remote sensing point of view, several near flybys of the NASA DC 8 and ER-2 provided supplemental interpretation data. Data are available from the online NASA Langley Research center mission database (http://www-air.larc.nasa.gov/missions/seac4rs/, last accessed in February 2016). The NASA DC-8 was fitted with the largest complement of atmospheric chemistry and aerosol instrumentation ever placed on a single aircraft. Especially relevant to the UW-HSRL deployment, a key instrument for the SEAC^{4}RS DC-8 was the NASA LaRC differential absorption lidar (DIAL) with enhanced HSRL capabilities. The ER-2 was also heavily outfitted for SEAC^{4}RS with a suite of in situ and remote sensing instruments, including the NASA Cloud Physics Lidar [*McGill et al*., 2002]. Because of airspace restriction, full vertical profiles over the Huntsville site were not possible, but the DC-8 was able to pass by in the vicinity on six occasions—12, 14, and 21 August and 6, 11, and 21 September. The NASA ER-2 performed overpasses directly over Huntsville on 12 and 21 August 2013.

2.4. Baseline HSRL Data Quality and Characteristics

After deployment the HSRL data set underwent a quality assurance exercise. This includes (1) evaluating the signal-to-noise characteristics of the aerosol backscatter profile including correcting the region where the telescope is out of focus (geometric overlap function) between the surface to ~5 km, (2) assessing the HSRL's ability to retrieve extinction and lidar ratio, and (3) providing an objective measure of how aerosol layers extend in the vertical. These are described in the following subsections.

2.4.1. Aerosol Backscatter

Perhaps, the HSRL's strongest capability is its ability to extract the aerosol backscatter profile to very high fidelity. Whereas a typical elastic backscatter lidar measures a combined molecular and aerosol signal, HSRL technology allows for the quantification of aerosol backscatter signals over an order of magnitude below Rayleigh. Calibration coefficients were evaluated using clear-sky regions near the observation times. This system was determined to have a precision in aerosol backscatter of better than 10^{-7} (m sr)$^{-1}$ for a 1 min average and 10^{-8} (m sr)$^{-1}$ for 15 min averages. In comparison, Rayleigh backscatter is 1.16e−5, 7.7e−6, and 4.4e−6 (m sr)$^{-1}$, at 1, 5, and 10 km. That is, in a comparable elastic backscatter scatter system, the aerosol backscatter precision is 1% of the total signal.

2.4.2. Derivation of Extinction and Lidar Ratio

The derivation of extinction measurements from HSRL systems can be complex—especially near the lidar aperture. To compute the aerosol or particulate extinction, it is necessary to compute the slope of the measured molecular signal, as any reduction in the amount the molecular signal must be from signal attenuation from particulates in the atmosphere. Of course, one must also account for the changing atmospheric density with altitude and attenuation from molecular scattering. An optical telescope's field of view (FOV) is controlled by the field stop, i.e., an aperture on the telescope focal plane, and the telescope focal length. Unlike in astronomy where all the observed targets are at very large distances away from the telescope, in lidar it is necessary to image the laser pulse propagating through the entire atmospheric column. For targets very close to the telescope, the image of the beam is out of focus and overfills the field stop; therefore, the measured signal at close ranges is much less than expected from the lidar equation. Because of the UW HSRL's small FOV, optical design, and system alignment, the "image" of the scattering volume is not fully in focus until a range of about 4.5 km from the system. From studying the system performance we have determined that the signal below 4.5 km in the so-called "overlap" region varies in time, sometimes hourly, during the daytime. Possible explanations for this variability could be atmospheric turbulence near the lidar system, i.e., heating from a large dark rooftop, and small optical misalignments from temperature changes within the lidar system. In any case, these fast-changing fluctuations must be corrected for before reliable aerosol extinctions can be measured close to the lidar system. Extinction derivations can be strongly influenced by slight changes in processing. The system used here is capable of accurate extinction measurements for aerosol/clouds with the extinction coefficient greater then 1×10^{-4} m^{-1} for altitudes greater than 4.5 km.

Because of the above considerations, and that the bulk of AOT and AOT variability is within 2 km of the surface, we chose to focus on aerosol backscatter rather than derivation of aerosol extinction. The backscatter cross section is essentially calculated from the ratio of the molecular and total backscatter channels; therefore, any range-dependent instrument effects are canceled out. Using an HSRL backscatter product is still superior to an elastic backscatter system, as estimates of light extinction are linearly related to lidar ratio—regardless of altitude. That is, for an assumed lidar ratio the error in derived extinction is linear in the error in that lidar ratio. For this overview paper, it is then simplest and most consistent to scale aerosol

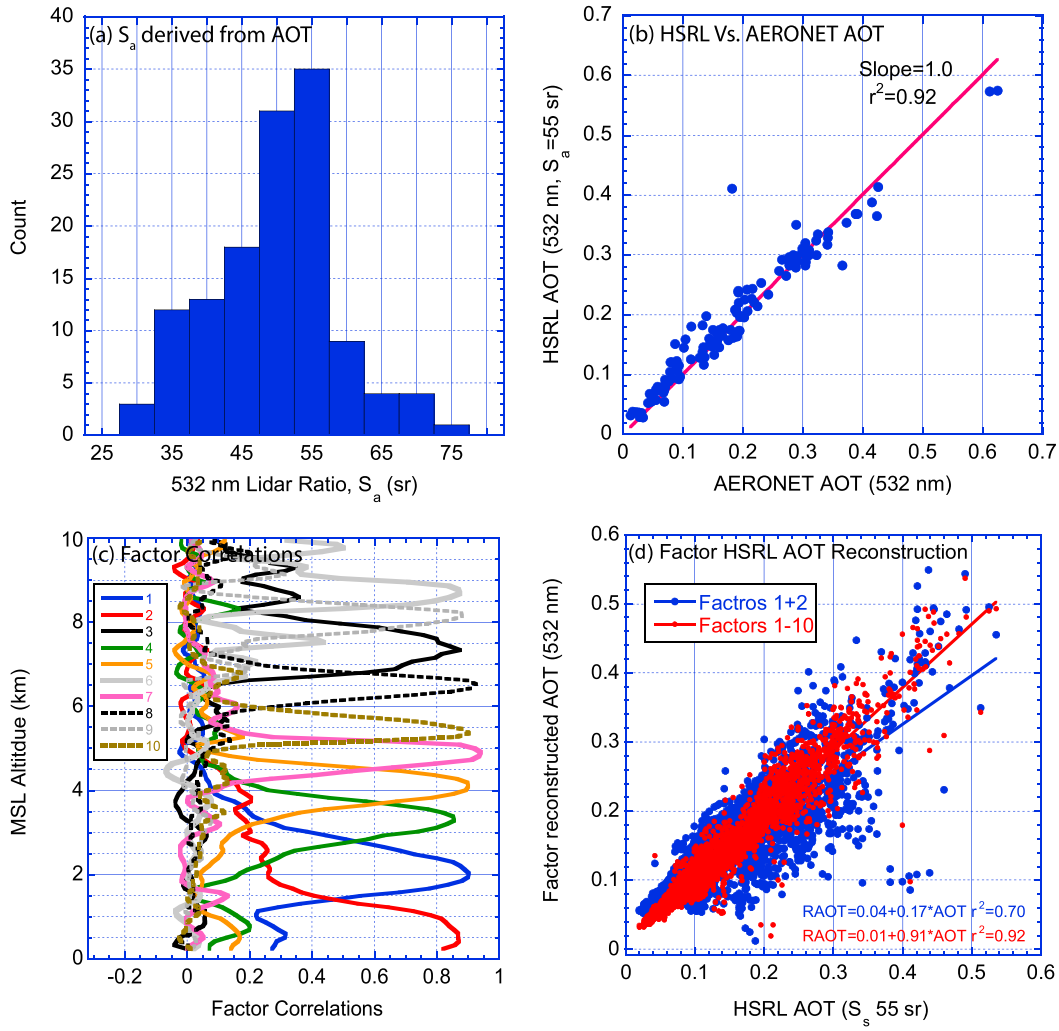

Figure 1. (a) Estimated lidar ratio (S_a) by comparing integrated HSRL aerosol backscatter to AERONET AOT. (b) Regression of HSRL inferred AOT using a static $S_a = 55$ sr compared to AERONET. (c) Altitude correlations to the PCA factors listed in Table 1. (d) Correlations of the factor reconstructed 532 nm AOT using $S_a = 55$ sr against the total HSRL integrated value for (blue) the first two factors and (red) the first 10 factors.

backscatter to extinction using some benchmark. Fortunately, the generation of extinction from aerosol backscatter is straightforward. To provide estimates of the extinction near the surface, one can assume a constant lidar ratio for a given aerosol species class, such as in the CALIOP retrieval, and thus, the aerosol backscatter scales linearly with extinction via the lidar ratio S_a. A histogram of derived S_a through the comparison of UW HSRL integrated aerosol backscatter to AERONET AOT derived at 532 nm (section 2.2) is presented in Figure 1a for all cases with successful level 2.0 Dubovik retrievals (this is used to ensure uniformity of sky condition). This is similar to what is done for NASA MPLnet [*Campbell et al.*, 2002]; although here the retrieval is purely on aerosol backscatter, not total scatter. Overall lidar ratios are reasonable for this environment with a modal value of 55 sr [e.g., *Ferrare et al.*, 2001; *Müller et al.*, 2007; *Burton et al.*, 2014], although somewhat lower than the value of 65 sr used by CALIPSO [*Winker et al.*, 2008]. Mean and standard deviation is 53 ± 18%. If we chose 55 sr as baseline lidar ratio for HSRL and compare to the AERONET cases, we get the regression in Figure 1b, with a unity slope and a high r^2 value of 0.92. Again, direct lidar ratio derivation from this system is a topic of future work. But, for the purposes of this overview paper, we will assume $S_a = 55$ sr for estimates of aerosol extinction for simple scaling, within nominally a 20% uncertainty in most cases based on one standard deviation from Figure 1a. Given the possible values for lidar ratios [e.g., *Burton et al.*, 2014], using a static 55 sr value can lead to 33% bias or

Table 1. Principle Component Analysis With Varimax Rotation Outcomes for Aerosol Backscatter[a]

Factor	Eigenvalue	Peak CorrelationAltitude (msl)[b]	Cumulative Variance explained-Backscatter	Cumulative Variance ExplainedAOT (55 sr)
1	26.5	2030 m	24%	35%
2	19.3	410 m	42%	71%
3	11.6	7340 m	52%	72%
4	7.3	8500 m	59%	81%
5	5.5	4200 m	64%	86%
6	4.8	8700 m	68%	88%
7	4.1	4730 m	72%	89%
8	3.2	8150 m	75%	90%
9	2.5	6440 m	77%	92%
10	2.3	5500 m	80%	92%

[a]Included are component eigenvalues, the peak correlation altitude, the cumulative variance in backscatter explained, and cumulative variance explained against inferred AOT assuming a lidar ratio of 55 sr.
[b]To convert from mean sea level (MSL) altitude to local above ground level (AGL), subtract 200 m.

extreme cases. This bias is noted in this paper and is visible as a linear difference between lidar derived AOT and its AERONET counterpart.

2.4.3. Objective Analysis for Vertical Partitioning

In addition to uncertainty in the lidar ratio, the complexity of aerosol features and vertical profiles defies easy parametrization. Different methods of lidar data dimension reduction and characterization are a topic of a future publication. However, to help guide analysis of this introductory paper, we performed a principle component analysis (PCA) with Varimax rotation on all 15 min cloud-free aerosol backscatter profiles with suitable signal to 10 km at 90 m resolution. This PCA analysis was performed in a manner similar to *Chew et al*. [2013] and objectively identifies orthogonal modes of variability in the vertical profile of aerosol backscatter. Here we use the component factors only as a rough guide to objectively define levels of aggregation and comparison. A total of 16 factors were extracted with eigenvalues greater than 1—a typical benchmark for PCA significance when the factor cannot be distinguished from random data at the 95th percentile. The first 10 factors are listed in Table 1 with altitude correlations shown in Figure 1c and eigenvalues above 2.5. These first 10 corresponded to 80% of total aerosol extinction variance. Generally, factors are spaced ~1600 and 2200 m near the surface, reducing to 200–900 m in the free troposphere. Such factors give a very rough indication of the vertical correlation lengths of aerosol layers. As is elaborated in sections 3 and 4, the first two factors represent mixed layer and entrainment zone planetary boundary layer (PBL) phenomenon. While capturing only ~42% of the extinction variance, they capture 71% of variance in integrated backscatter or AOT if one assumes a constant S_a (Figure 1d). Factors 3 and 6, 8, and 9 represent significant upper free tropospheric smoke layer intrusions. Factors 4, 5, and 7 represent convective outflow or biomass burning transport. Factors 1–10 explain 80% of the variance in aerosol backscatter but 92% of the variance in inferred AOT, demonstrating that AOT is well reconstructed. Outliers in Figure 1b are largely due to short durations transients in the upper free troposphere and represented in Factors 11–16 with generally low correlations (below 0.4) or represent only a few data points and hence not shown here. We then aggregate layer integrated backscatter (i.e., layer AOD with a constant lidar ratio of 55 sr) at the overlap points of the strongest factors, namely, 1.4 km, 2.8 km, 3.7 km, 4.5 km, 5.5 km, and 5.5–10 km msl (keeping in mind that the lidar transmitter is at 220 m). In certain rare occurrences, smoke was also detected above 10 km. But, due to the low signal in general in this altitude regime, they are excluded from the bulk analysis. These are discussed in section 4.2.

3. Results—I: Overview of Observed Aerosol Environment

In this first of two results sections, we provide an overview of the environment experienced by the UW-HSRL during its Huntsville deployment. We begin with mean monthly profiles of aerosol backscatter with supporting AOT and particulate matter data (section 3.1), followed by an in-depth analysis of a canonical fair weather day, 27 August 2013 to aid in interpretation of the basic features of the monthly average profiles and the dominant modes of variability as defined by the PCA analysis (section 3.2). We finalize this section with a time series analysis of the monitored environment to demonstrate daily variability (section 3.3).

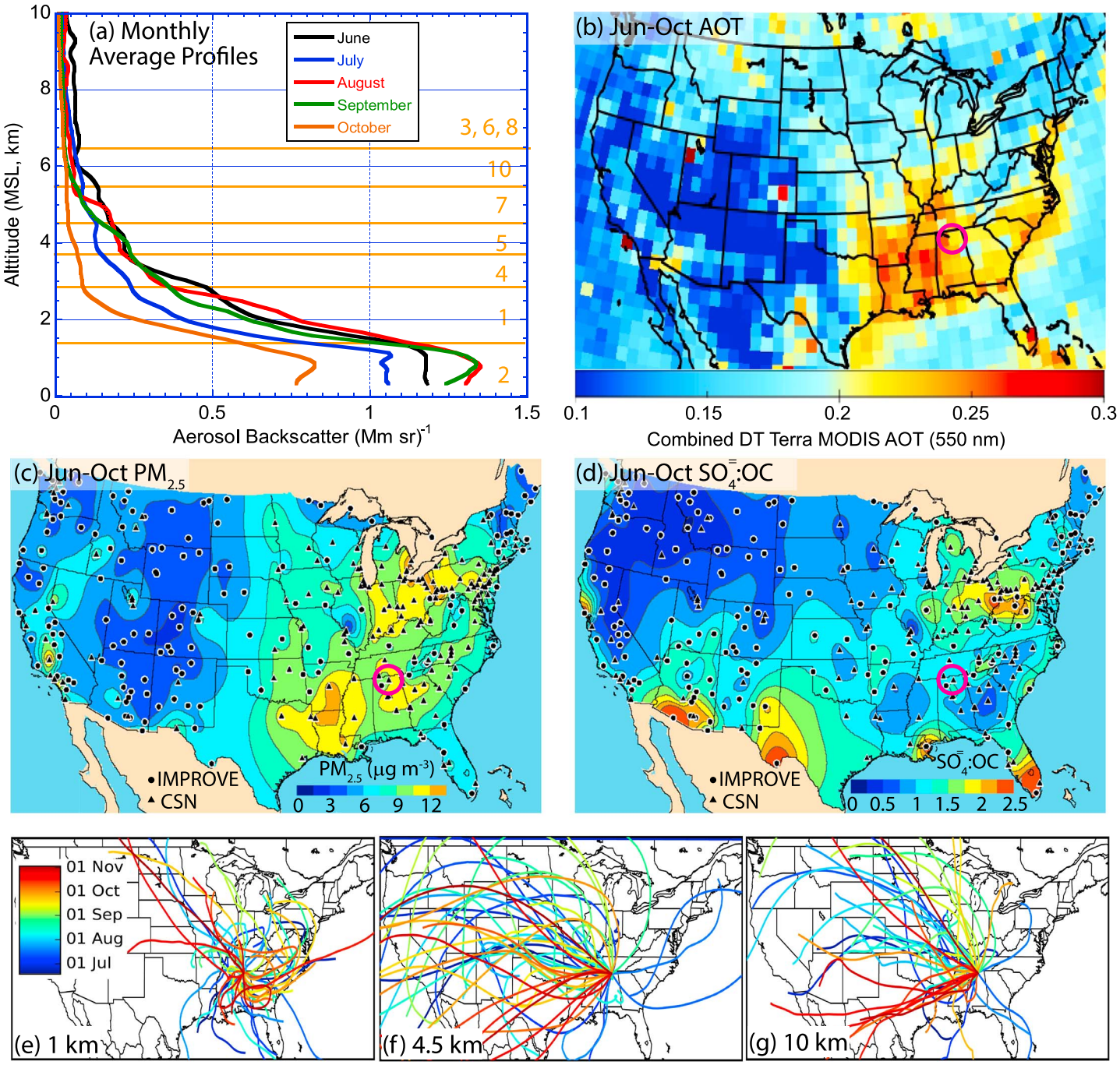

Figure 2. Summary continental United States data for the June–October 2013 study period. Included are (a) monthly average aerosol backscatter profiles for all cloud-free HSRL measurement profiles to 10 km, with crossover points for PCA factors marked in orange. (b) Aerosol optical thickness form the Terra MODIS level 3 combined dark target MODIS product. Marked in a circle is the Huntsville, AL, site. (c) Krigged composite of $PM_{2.5}$ and the ratio of sulfate to organic carbon based on CSN and IMROVE filter data from the method of *Hand et al.* [2012]. (e–g) HYSPLIT back trajectories every 3 days for 1 km, 4.5 km, and 10 km, respectively.

3.1. The 2013 Summer Season Aerosol Properties

3.1.1. Monthly Average Vertical Profiles

To provide a reference on aerosol vertical profiles in the SEUS during the UW-HSRL deployment, the monthly composite of all cloud-free aerosol backscatter profiles from 390 m to 10 km msl altitude for 19 June to 31 October 2013 is provided in Figure 2a. Key monthly parameters are similarly listed in Table 2. Overlaid on Figure 2a are the layers associated with the dominant 10 factors, with lines signifying the

Table 2. Pairwise Calculations of Mean and Standard Deviation of AERONET Total AOT, AERONET Fine Mode AOT, 440–670 nm Angstrom Exponent, Surface $PM_{2.5}$, HSRL Integrated Backscatter Inferred AOT (Assuming $S_a = 55$ sr), and Aerosol Backscatter by Layer

	June	July	August	September	October
532 nm AOT	0.18 ± 0.09	0.16 ± 0.05	0.26 ± 0.08	0.18 ± 0.15	0.10 ± 0.06
532 nm fine AOT	0.13 ± 0.07	0.15 ± 0.05	0.23 ± 0.08	0.17 ± 0.14	0.09 ± 0.06
Ångstrom exponent	1.53 ± 0.19	1.74 ± 0.21	1.6 ± 0.19	1.87 ± 0.16	1.82 ± 0.16
$PM_{2.5}$ ($\mu g\ m^{-3}$)	13 ± 3	11 ± 3	15 ± 4	15 ± 5	10 ± 4
		Average Backscatter			
Inferred AOT (55 sr)	0.19 ± 0.06	0.14 ± 0.04	0.19 ± 0.06	0.17 ± 0.10	0.09 ± 0.04
<1.4 km $(Mm\ sr)^{-1}$	1.17 ± 0.35	1.02 ± 0.41	1.29 ± 0.40	1.25 ± 0.65	0.75 ± 0.41
1.4–2.8 km	0.67 ± 0.28	0.41 ± 0.15	0.74 ± 0.47	0.58 ± 0.64	0.08 ± 0.17
2.8–3.7 km	0.34 ± 0.14	0.20 ± 0.15	0.29 ± 0.19	0.30 ± 0.27	0.08 ± 0.06
3.7–4.5 km	0.21 ± 0.12	0.13 ± 0.12	0.20 ± 0.21	0.21 ± 0.23	0.06 ± 0.04
4.5–5.5 km	0.15 ± 0.12	0.10 ± 0.09	0.13 ± 0.20	0.10 ± 0.1	0.04 ± 0.01
5.5–10 km	0.06 ± 0.05	0.04 ± 0.03	0.04 ± 0.02	0.03 ± 0.01	0.02 ± 0.01
		Layer Fraction			
<1.4 km	0.45 + 0.07	0.52 + 0.12	0.48 + 0.09	0.56 + 0.13	0.58 + 0.13
1.4–2.8 km	0.27 + 0.08	0.23 + 0.06	0.27 + 0.10	0.20 + 0.11	0.22 + 0.10
2.8–3.7 km	0.10 + 0.02	0.09 + 0.06	0.09 + 0.05	0.09 + 0.04	0.07 + 0.04
3.7–4.5 km	0.06 + 0.02	0.04 + 0.03	0.04 + 0.05	0.05 + 0.04	0.03 + 0.02
4.5–5.5 km	0.04 + 0.02	0.04 + 0.03	0.04 + 0.05	0.04 + 0.04	0.03 + 0.01
5.5–10 km	0.08 + 0.05	0.08 + 0.04	0.06 + 0.03	0.06 + 0.04	0.07 + 0.06

overlap point of correlation between adjacent factors (again, only as a rough guide to identify modes of variability and likely levels of aggregation). As discussed in section 2, these aerosol backscatter profiles are linearly related to aerosol extinction through the lidar ratio (S_a). Assuming a baseline S_a of 55 sr, the scale along the abscissa is equivalent to an extinction coefficient of ~0.08 km^{-1}. Aerosol S_a values range from ~35 for dust and sea salt to ~70 for smoke. Thus, any given profile extinction may deviate by nominally one third. The monthly average profiles of aerosol backscatter are similar to many such light scattering or extinction profiles in the literature from in situ aircraft and airborne lidars in polluted North American regions [e.g., *Cohn and Angevine*, 2000; *Shinozuka et al.*, 2007; *Clarke and Kapustin*, 2010; *Drury et al.*, 2010; *Ziemba et al.*, 2013] including airborne composites from SEAC^{4}RS [e.g., *Kim et al.*, 2015; *Wagner et al.*, 2015]. Aerosol backscatter is dominant at the surface to ~ 1.5 km (Factor 2), decreasing rapidly to ~ 3.5 km (Factor 1). A plateau occurs from ~3–6 km (Factors 5, 7, 9, and 10). Average aerosol backscatter flattens out to cleaner conditions above 5.5–6.5 km msl. However, while the upper free troposphere appears to exhibit low average values, occasional but strong aerosol layers occurred, as described in Factor 3 and other occasional layering phenomenon as described by Factors 4, 6 and 8. Above 10 km was usually pristine, except for isolated events of biomass burning smoke just below the tropopause as discussed in section 4.3.

While monthly profiles are roughly similar in shape, there is variability within levels. Monthly average near-surface backscatter was roughly 1.2, 1.15, 1.4, 1.25, and 0.8 $(Mm\ Sr)^{-1}$ for June, July, August, September, and October, respectively. Assuming a baseline S_a of 55 sr, these correspond to light extinction values of roughly 0.07, 0.06, 0.08, 0.07, and 0.04 km^{-1}. In comparison, monthly average AOTs from AERONET were 0.18, 0.16, 0.26, 0.17, and 0.10 for June through October, highly correlated with near-surface backscatter ($r^2 = 0.8$)—consistent with AOT being dominated with boundary layer aerosol species. Corresponding monthly $PM_{2.5}$ values from filters analyzed from the local CSN site for June through October were 13, 10, 13, 14, and 10 $\mu g\ m^{-3}$, respectively. At the monthly level correlations between $PM_{2.5}$, AOT and near-surface backscatter are also good, with r^2 values of 0.7 and 0.89, respectively. However, we show correlations diminish rapidly at higher temporal resolution.

Also from Table 2 it is clear that though the free troposphere was low in magnitude in aerosol backscatter relative to the PBL environment, the free troposphere did exhibit a great deal of variability. Standard deviations of aerosol backscatter were 50–100% of the mean. Significant enhancements were observed in June and August, as discussed in part due to the transport of smoke from the western United States as well as some regional convective pumping in August. An example of such features is provided in section 4.3.

3.1.2. Regional Context of the Huntsville Site

The Huntsville site was well positioned for representative monitoring of the SEUS' regional aerosol environment in 2013. As discussed in the SEAC^{4}RS overview paper [*Toon et al*., 2016], the average summertime meteorological pattern for the study consisted of a seasonally strong quasi-stationary ridge and trough pair in the western and eastern United States, respectively. Consequently, the SEUS exhibited considerable summertime convective activity, with typically significant boundary layer cumuliform cloudiness and periods of deep convection. In this pattern, boundary layer "regional pollution" in the SEUS was joined by Pacific Northwest biomass burning smoke transported in the free troposphere around the ridge into the eastern and southeastern U.S. Within the SEUS, high summertime temperatures led to biogenic emissions, that when combined with anthropogenic emissions lead to regional aerosol enhancements—reflected in the high aerosol backscatter in the PBL. By the end of the SEAC^{4}RS mission, the SEUS environment shifted from the quasi-stationary features to more fall-like weather patterns of traveling waves and frontal activity. Temperatures dropped, as did biogenic emissions—also in part reducing aerosol loadings as reflected in Figure 2a.

The regional representativeness of the Huntsville site is further demonstrated in Figure 2, including a Continental U.S. (CONUS) June through October averaged Terra MODIS combined dark target AOT (Figure 2b), as well as regional $PM_{2.5}$ surface concentrations for the same period (Figure 2c) and ratios of sulfate to organic carbon from combined Interagency Monitoring of Protected Visual Environments (IMPROVE and CSN site data—Figure 2d, e.g., derived from the same Kriging method as *Hand et al*. [2012, 2014]. The Huntsville site is marked by a circle in Figure 2 . To demonstrate variability across the summer, monthly average maps of Terra MODIS combined dark target AOT for June through October are also given in Appendix Figure A1. From Figures 2 and A1 key aerosol features are visible over CONUS. SEUS haze dominated CONUS AOT for the 2013 summer months, with particular enhancement up the Mississippi Valley and into the Ohio River Valley. Average surface $PM_{2.5}$ also shows similar patterns, with perhaps some enhanced $PM_{2.5}$ relative to AOT in the Ohio River Valley. The ratio of sulfate to organic carbon has a strong north-south gradient, consistent with the heavy industry and power plant emission in the north [*Hand et al*., 2012, 2014] and petrochemical plus biogenic emissions in Houston through coastal Louisiana and Arkansas [*Chalbot et al*., 2013]. From Arkansas and Mississippi through the Carolinas much of the aerosol mass is organic dominated, enhanced from secondary aerosol production through anthropogenic and biogenic processing [e.g., *Weber et al*., 2007; *Hidy et al*., 2014; *Xu et al*., 2015]. As discussed in *Hand et al*. [2012] the sulfate to organic carbon ratio averaged ~1 with factor of 2 departures commonplace.

Biomass burning also has a strong influence on CONUS and Huntsville AOTs. Some of the AOT enhancement up the Mississippi Valley is likely of agricultural burning origin [e.g., *McCarty*, 2011; *Lin et al*., 2014; *Toon et al*., 2016]. Also, in 2013 a clear aerosol lobe is also visible from Northeast Texas through Arkansas, a likely mix of petrochemical, biogenic, and agricultural biomass burning. Monthly average AOTs in Figure A1 demonstrate that at times AOT was strongly enhanced across CONUS due to the significant biomass burning season—particularly in Colorado in June and California through Idaho in August. Slight enhancements are also visible in the surface concentrations from the combined CSN and IMPROVE stations in a transect from central California to Idaho and in eastern Colorado. As expected for biomass burning, the organic fraction is high. The SEUS summer 2013 meteorology is often dominated by a western high-pressure system-lofted smoke transported eastward into the SEUS [e.g., *Toon et al*., 2016]. This is especially visible in June and August AOT (Appendix Figures A1a and A1c) and corresponding enhancements in mean aerosol backscatter in the 3–6 km lidar data in Figure 2a.

Detailed trajectory analyses are outside the scope of this paper, but we can quickly relate the regional aerosol characteristics directly to the Huntsville site through the use of 72 h HYSPLIT back trajectories. Trajectories spawned every 3 days for the upper mixed layer (1 km msl) midfree troposphere just below the 0°C melting level (4.5 km) and upper troposphere (10 km) in Figures 2e–2g, respectively. Additional trajectories every 12 h broken down by month are also provided in Appendix Figure A2 at five levels: 1 km for the mixed layer, 3 km just above the top of the PBL, 4.5 km just below the melting level of 0°C, 7 km in the midtroposphere, and 10 km at the upper troposphere. Data are also provided at the monthly level as well as for the last 2 weeks of June when the HSRL came into operation. At lower levels (1 and 3 km), trajectories indicated that PBL air could potentially arrive from practically anywhere in the eastern and Southeast United States. In September there was a stronger proclivity for low-level air to be from the northeast. Thus, we can assume that for the purposes of this overview the PBL was dominated by particles of anthropogenic pollution and

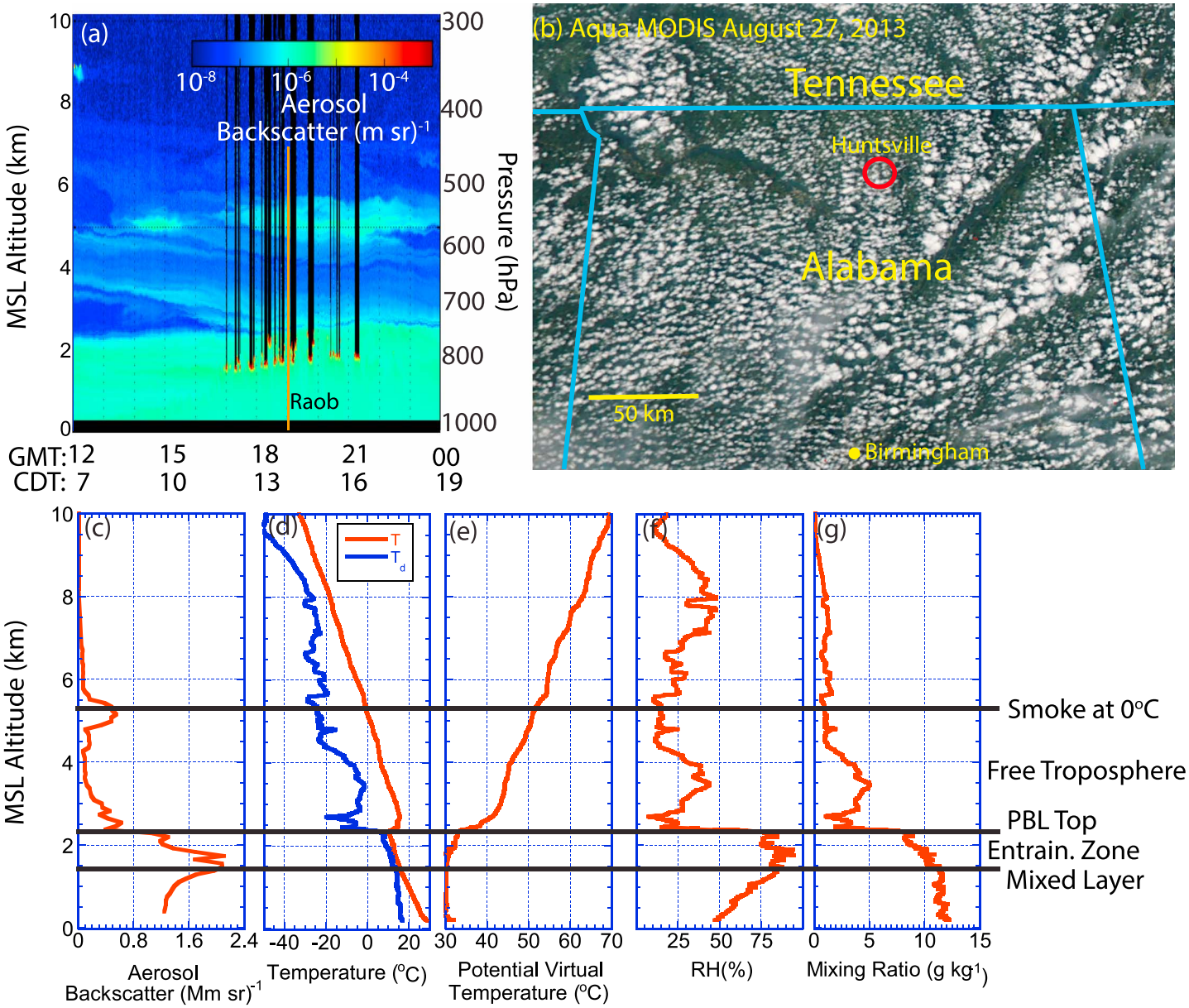

Figure 3. (a) UW-HSRL aerosol backscattering time-height cross section for the morning through late afternoon of 27 August 2013. Radiosonde release at 18:30 is marked as an orange line. (b) Corresponding Aqua MODIS image of the region at ~18:30 UTC/13:30 CDT. (c) Aerosol backscatter profile for the 18:30 UTC radiosonde release. Radiosonde profiles of (d) temperature and dew point, (e) potential virtual temperature, (f) relative humidity, and (g) water vapor mixing ratio.

biogenic origin with perhaps some occasional regional agricultural burning. At free troposphere altitudes, air masses were more dominated by transport from the western United States and Pacific Northwest as air wrapped around the southwest monsoon and frequently brought western wildfire smoke to the region [e.g., *Toon et al.*, 2016].

3.2. Description of the Fair Weather Base State of 27 August 2013

The nature of HSRL data and the representativeness of the seasonal mean in Figure 2 and the discussion of section 3.1 require an understanding of instantaneous state profiles. To this end, the example of 27 August, 2013 12–24 Z (7:00–19:00 CDT) is provided in Figure 3. Day 27 August 2013 was typical of most days during the more convectively active late June through mid-September portions of the deployment. Fair weather boundary layer clouds at 30–70% coverage develop and midday through the afternoon with isolated

Thunderstorms (CBs) in the area. Breaks from this pattern were related to significant convective activity associated with weak cold fronts entering the area or areas of moisture transported from the Gulf Coast. An example of this environment during more enhanced convective conditions is provided in detail in section 4.1. By late September, the region transitioned to a more fall-like frontal activity (section 4.2). Day 27 August lacks cirrus at Terra and Aqua overpass time, resembles the mean August profile presented in Figure 2a, and also clearly demonstrates key aerosol layering and thermodynamic features common at the Huntsville site. Further, on this day a midtropospheric biomass burning layer advected to the region from Pacific Northwest biomass burning. Taken together, 27 August 2013 is close to the "median" environment experienced by SEAC^{4}RS and thus is a good day to describe common features observed in lidar data.

To demonstrate the UW HSRL's ability to monitor the diurnal aerosol and cloud environment, included in Figure 3a is a 12 h time-height segment of HSRL attenuated aerosol backscatter, for the daylight hours of 12–24 Z (7 A.M.–7 P.M. CDT). To add context, Aqua MODIS RGB for 18:30 UTC/13:30 CDT is provided in Figure 3b showing this to be a fair weather day as noted with associated 50% fair weather cumulus (i.e., cumulus humilis or CuHu to cumulus mediocris or Cu). This is followed by an aerosol backscatter profile at the SEACONS radiosonde release at 18:30 UTC (Figure 3c, profile marked in orange on Figure 3a) as well as sonde thermodynamic quantities of Figure 3d temperature and dew point, (Figure 3e) virtual potential temperature, (Figure 3f) relative humidity, and (Figure 3g) water vapor mixing ratio. Labeled are key tropospheric layers and levels. On this day, AERONET AOT at 532 nm was ~0.18 in the morning hours. By midday, a 0.12 AOT enhancement occurred due to the advection of smoke at ~ 5 km msl. Surface $PM_{2.5}$ however was more constant 14–18 $\mu g\ m^{-3}$, largely uncorrelated with HSRL derived AOT over the day (not shown, $r^2 = 0.13$).

There is a long history of interpreting PBL structure from lidar data [e.g., *Kaimal et al.*, 1976; *Boers et al.*, 1984; *Piironen and Eloranta*, 1995; *Cohn and Angevine*, 2000; *Brooks*, 2003], and Figure 3 clearly shows PBL dynamics and the primary sets of aerosol layer expected in this environment. Starting at the surface, a 100–200 m deep surface layer exchanges heat, momentum, and atmospheric constituents between the atmosphere and the surface [e.g., *Arya*, 1988; *Stull*, 1988]. This layer is typically oscillating between statically neutral and unstable diurnally, due to radiative cooling and heating at the surface, respectively. Given that this particular HSRL becomes quantitative ~200 m above the telescope (~390 m msl in the HSRL data), the dynamics of the surface layer are difficult to systematically monitor in this data set, although the temperature structure of the surface layer is visible periodically in the lidar and radiosonde temperature data (e.g., Figures 3d and 3e). At nighttime, the surface layer is mixed largely by periodic surface drag induced turbulence dampened by the statically stable environment due to radiative cooling at the surface. As the Sun rises and heats the surface thermal turbulence begins to form [e.g., *Kaimal et al.*, 1976; *Angevine et al.*, 2001]. The resulting mixed layer above the surface layer is clearly visible in the lidar data: mixed layer topped fair weather cumulus clouds from late morning through late afternoon. In such a well-mixed environment, water vapor is conserved (e.g., water vapor mixing ratio is static in Figure 3g), yet temperature drops adiabatically (Figures 3d and 3e), and thus RH increases with altitude (Figure 3f). As the "mixed layer" is mixed in regard to aerosol particle mass as well, the increase in RH with altitude results in a nonlinear increase in aerosol backscatter and extinction due to particle hygroscopicity (Figures 3c and 3f). Often the first maximum in aerosol backscatter is taken as an indicator of the height of the mixed layer [e.g., *Boers et al.*, 1984; *Piironen and Eloranta*, 1995; *Brooks*, 2003]. In the late morning through early afternoon, the mixed layer deepens, and turbulence at the interface erodes into the free tropospheric air aloft. As buoyant air mixes with the neutral to stable air in the free troposphere an inversion is created at the top of the mixed layer, forming the base of an entrainment zone as the start of the interface with the free troposphere (e.g., see lidar observations of *Boers and Eloranta* [1985]).

In the midmorning through midafternoon when the mixed layer grows to sufficient depth to allow saturation at the inversion, the entrainment zone is enhanced by the formation of convective clouds. In this case, based on the lidar and the MODIS cloud product, 1 km deep CuHu are formed by individual thermals. These cloud tops largely mark the top of the PBL. In this particular case, a large 10°C subsidence inversion at 3 km strongly caps the development of clouds and the PBL. Indeed, for fair weather boundary layer conditions by nature, the free troposphere is usually stable to weakly conditionally unstable with a strong subsidence inversion (else, it would not be fair weather). This strong inversion is well marked not only by the temperature but also by aerosol backscatter, relative humidity, and water vapor mixing ratio. As the afternoon progressed and clouds develop, aerosol backscatter indicates clouds eroding this inversion, but, given the inversion

strength, only by several hundred meters. At sundown, thermal forcing from the surface is diminished, and the mixed layer collapses as forcing is reduced to residual heat from the surface and shear turbulence. The previous days mixed layer air is then sequestered aloft. In the absence of aerosol emission at the surface, the overall vertical profile can appear relatively stable through the night. Alternatively, in the presence of surface sources, a strongly polluted surface layer can form. In the presence of radiative cooling, relative humidity can increase, and through aerosol hygroscopicity, increase extinction further.

The PBL features described are well represented with Factor 2 (Figures 1c and 2a), the dominant factor on this day. This factor includes the increase in backscatter with altitude in the mixed layer, and some lingering correlation with the entrainment zone. However, as will be discussed in section 3.3, the dominant variability in vertical extinction for the entire data set is Factor 1, which includes the addition of cases of deep PBLs with convectively active entrainment zones as well as some residual layers just above the PBL. In this case of simple fair weather PBL, Factor 1 scored near zero. Thus, Factor 2 represents a reasonable base state of PBL variability.

Above the PBL is the free troposphere. Between ~2.5 and 4.5 km many thin aerosol layers exist, decreasing in altitude with time—perhaps related to subsidence or other large-scale synoptic scale dynamics coupled with wind shear. Most notably, however, is a strong return at a height of ~ 5 km, which, based on AERONET and the use of 55 sr lidar ratio, has a layer AOD of ~0.12. This led to the free tropospheric Factors 7 and 10 as the remaining significant factors for this day. Trajectories from Figure 2 suggest smoke originated from the Pacific Northwest fires, perhaps even the California Rim Fire [*Peterson et al*., 2015; *Yu et al*., 2016]. Sampling of the DC-8 in the northwest on 27 August [*Toon et al*., 2016] detected evidence of fire trace gases and aerosol products, which circulated toward Huntsville around a high-pressure system. It was also found, using a tracer version of GEOS-5 [*Ott et al*., 2016], that 10–15% of elevated free tropospheric ozone over Huntsville had stratospheric origins. For the month of August, the biomass burning signature is well pronounced at ~5 km as demonstrated here (Figure 2a), the approximate height of the of the 0°C level. This level is well known to host a level of enhanced stability in convective environments [e.g., *Johnson et al*., 1996, 1999]. Above the 5 km smoke layer, the atmosphere is largely clear, with the notable exception of a thin cirrus layer at 9.5 km/12 Z. While under these pristine conditions, the HSRL cannot independently derive a lidar ratio, it can detect aerosol backscatter at the 10^{-8} to 10^{-7} $(\mathrm{m\,sr})^{-1}$ level. Given the range of likely lidar ratios, the corresponding to precision in estimated extinction values is on the order of ~0.007 km^{-1}.

The case of 27 August 2013 also provides an example of the synergistic use of aerosol and ozone data available to the science community. While the ozone lidar was only run sporadically during the mission, there are a number of cases of observations of enhanced ozone in smoke layers aloft. Figure 4 presents a 20 h period where the ozone lidar was also collecting data. Both the ozonesonde and ozone DIAL suggest an enhanced (~20 ppbv) ozone layer between 4 and 7 km, due to the high emissions of ozone precursors from the smoke [*Jaffe and Wigder*, 2012]. This smoke layer had enough moisture (RH > 10% in Figure 3f) to exclude it as a fresh stratospheric source. Ozone in the PBL, 50–60 ppb, was slightly lower than the seasonal average [*Newchurch et al*., 2003] in spite of a moderate aerosol loading, suggesting that the smoke transport in the free troposphere did not significantly affect the PBL at this time.

While Figure 3 provides an overview of the atmospheric aerosol and thermodynamic structure, considerable fine-scale features are present that are not visible in the figure or factors. In particular, the combined lidar and radiosonde data show remarkable detail and complexity in the PBL's aerosol and entrainment environment. This is demonstrated in the enhanced and annotated lidar image in Figure 5a, where we cropped the Figure 3 image from 16:00–22:00 UTC (11:00–17:00 CDT) and below 3 km, and adjusted the color bar. Associated temperature/dew point and relative humidity and mixing ratio profiles are also given in Figures 5b–5d, respectively. Also shown are the Aqua MODIS cloud top (Figure 5e) heights and (Figure 5f) temperatures corresponding to the RGB image in Figure 3b. Annotations depicting the mixed layer, residual layers and the entrainment zone are marked as is the time of the radiosonde release in Figure 5a. In the late morning the mixed layer grew rapidly by thermals, with an entrainment zone functionally confined to the interface. The mixed layer reached saturation at 17:00 UTC, forming CuHu (local noon and this point forward, we nominally designate the height of the mixed layer as cloud base). Driven by latent heat, clouds quickly expand the entrainment zone and functionally define the height of the PBL. This process is clearly visible in the time period of 17:00–19:00 UTC when at 19:00 UTC the entrainment zone growth is stopped by the subsidence inversion which in turn functionally defines the height of the full PBL. In the entrainment zone, moist mixed layer

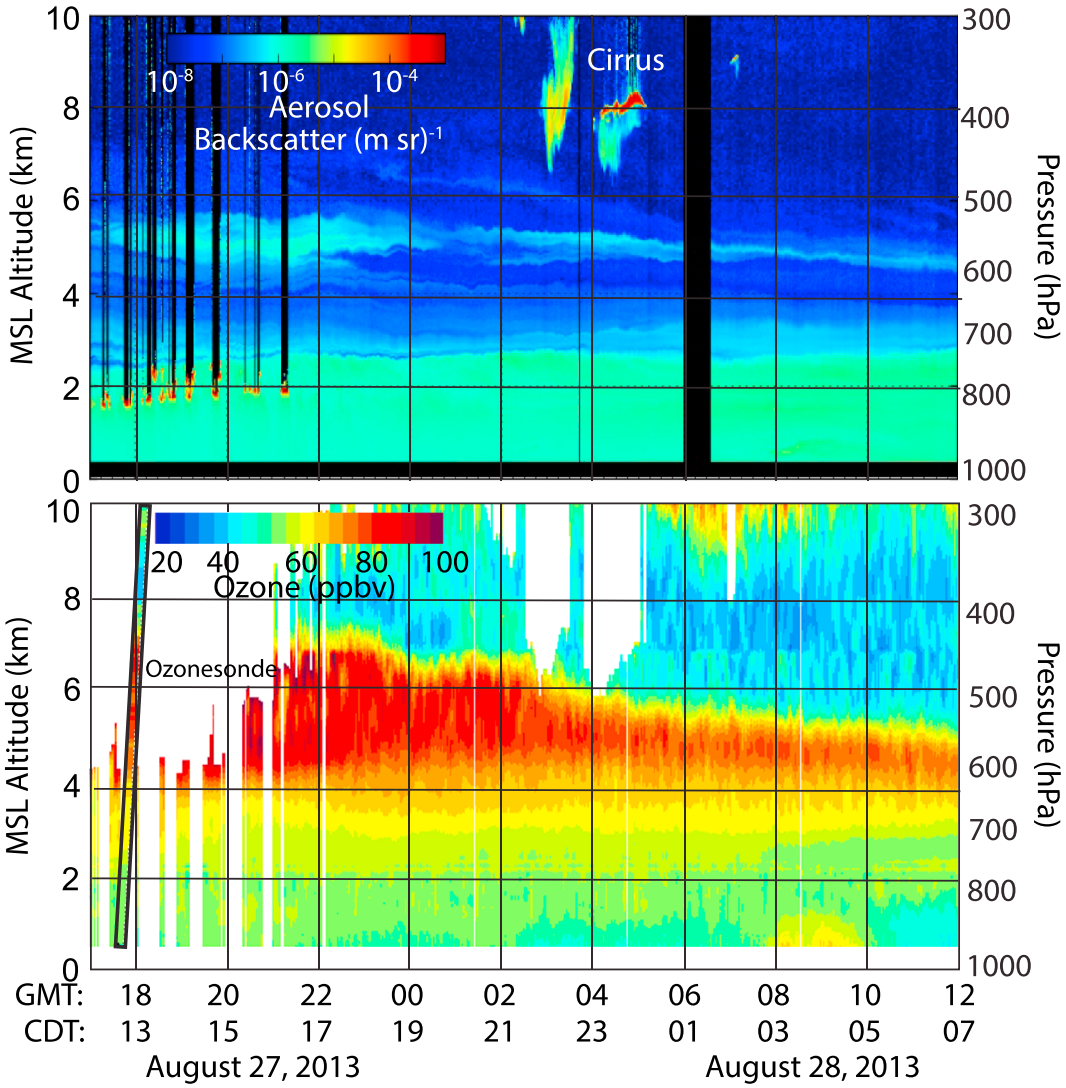

Figure 4. A 20 h period of simultaneous HSRL and ozone lidar data collection that includes the example day period of Figure 3. This period corresponds to a ~5 km smoke layer over a classic southeast U.S. boundary layer.

air injected by clouds exchanges with dry free tropospheric air subsiding on cloud edges. This manifests itself in a decrease in water vapor mixing ratio between the top of the mixed layer and the regional free tropospheric inversion in Figure 2g. In Figure 5a, however, we can actually see in the UW HSRL data the detrainment of water vapor and aerosol particles from clouds in the entrainment zone. Indeed, at 20:20 UTC an isolated aerosol feature is visible, likely due to an evaporating cloud top or residual halo. Similarly, clear aerosol backscatter striping is visible in the mixed layer between profiles under clouds and adjacent clear air. These aerosol enhancements below clouds are due to individual moist thermals working their way up the mixed layer. The increased RH of these rising thermals causes aerosol particles to hygroscopically grow. Conversely, continuity forces adiabatic warming and drier downdrafts between clouds. Within the entrainment zone, between "cloud" and "clear," lies cloud halos where the cloud moisture mixes with the drier air [*Radke and Hobbs*, 1991; *Twohy et al.*, 2009; *Tackett and Di Girolamo*, 2009]. Finally, aerosol layers are found in the entrainment zone, often coincident with the level of clouds formed at 2.1 km. This demonstrates that the entrainment zone has layering structure as well as bubbles of exchanging mixed layer and free tropospheric air.

A second cloud layer is also visible in the entrainment zone at 18:30 Z onward with a base at ~2.1 km msl. Similar multiple cloud returns in the entrainment zone were reported in the 2007 cumulus humilis aerosol

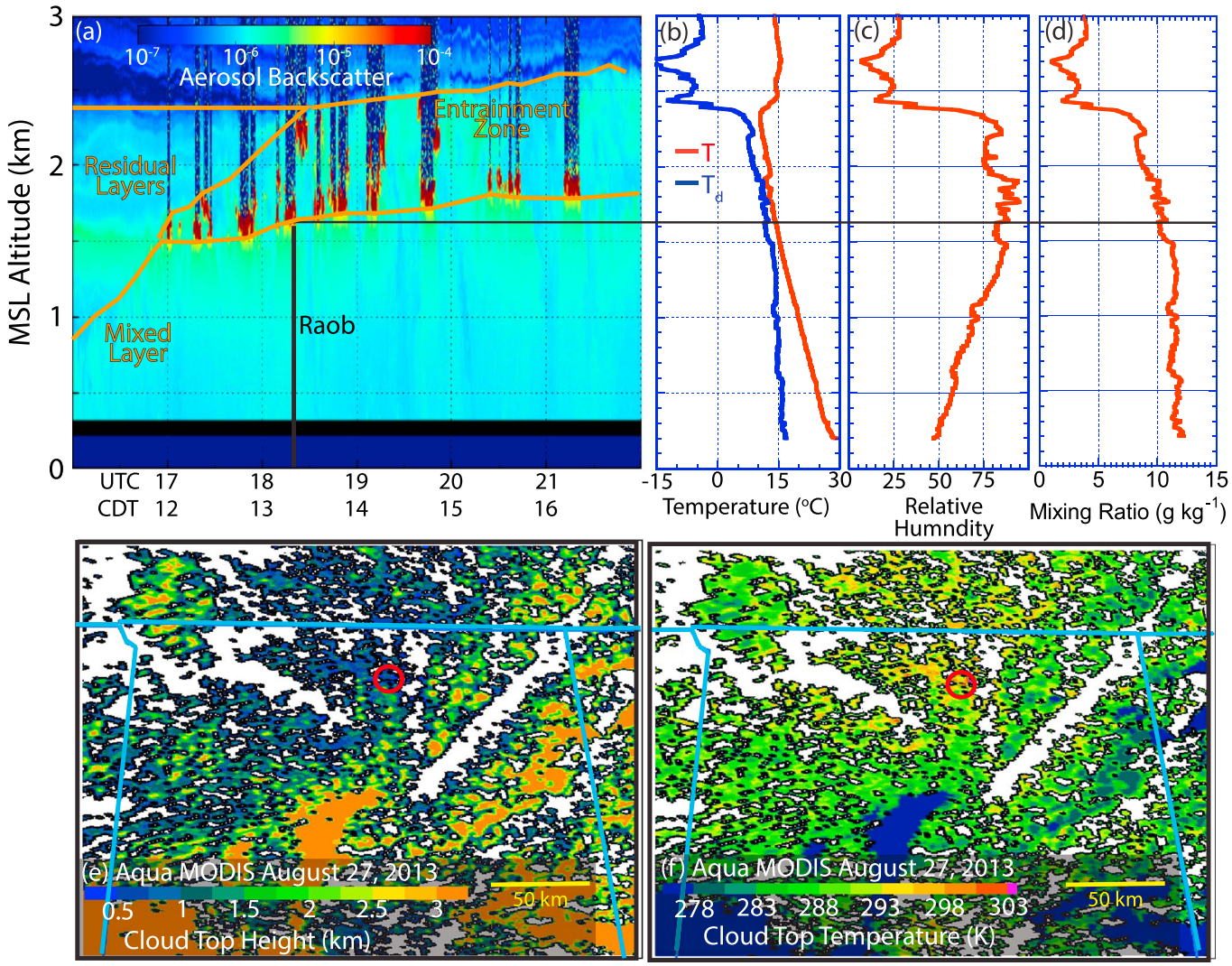

Figure 5. Rescaled and annotated data presented in Figure 3 to enhance visibility of key PBL features. (a) UW-HSRL aerosol backscatter, (b) temperature and dew point, (c) relative humidity, and (d) water vapor mixing ratio. Also shown are the Aqua MODIS cloud top (e) heights and (f) temperatures over the same area as in Figure 3b.

processing study [e.g., *Berg et al.*, 2009, Figure 4]. One may perhaps simply classify these clouds as edge effects due to wind shear or cloud growth or as CuHu and attribute their level to simple inhomogeneity in the PBL. However, one must also consider that these clouds owe their formation to mechanisms associated with detrainment from evaporating clouds, which, in the presence of cloud field inhomogeneity, leads to aforementioned layering structure. Potentially, altocumulus (Ac) may be forming at the top of the PBL. A key distinction is that these types of clouds form from injections of moisture from the tops of clouds forming below, perhaps leaving moisture layer or halos which in turn bring humidified aerosol particles with them [*Radke and Hobbs*, 1991; *Lu et al.*, 2003: *Twohy et al.*, 2009]. From a passive satellite perspective, they can be mistaken as cloud tops of deeper cumulus. However, using space-based lidar, they are more observable and have been shown to be prevalent in convectively active environments such as the summertime SEUS [*Sassen and Wang*, 2012].

The UW-HSRL's "bottom" up perspective to the cloud fields also provides insight into uncertainties in passive remote sensing of cloud properties. Ideally, one could infer cloud thickness by comparing cloud base from the HSRL to cloud top from satellite. In the case of MISR, direct parallax measurements of cloud tops can be measured to ~250 m resolution. Other passive satellites must rely on infrared estimates. However, for small boundary layer clouds such as this case, edge effects and atmospheric correction biases can be

significant [*Platnick et al*., 2016]. This is demonstrated in the 1 km Aqua MODIS cloud retrievals in Figures 5e and 5f. On this day at the radiosonde release time, MODIS was retrieving cloud tops at 0.3 to 1.8 km msl within 0.1 km of the site and with a mean value of 1 km. These retrieved values can be seen in the lidar imagery to be below the cloud base. Peaks for larger clouds away from Huntsville are more reasonable, capping at 3 km, at the subsidence inversion. The GOES product showed similar results, with cloud tops on par with MODIS. Comparing radiosonde temperatures to cloud temperatures shows that the system is consistent with regard to temperature. We thus attribute some of these differences to edge effects of smaller clouds. This said even for uniform stratocumulus (Sc) clouds, errors in cloud top can be >1 km [e.g., *Garay et al*., 2008; *Marchand et al*., 2010].

3.3. Time Series of the Overall Aerosol Environment During the HSRL Deployment

In section 3.1, monthly average aerosol backscatter profiles were presented and then explained through the use of a midday period of 27 August 2013 in section 3.2. Using these as a template, here we briefly provide a synopsis of the aerosol environment through a bulk time series analysis. Figure 6 presents a time series of key environmental variables for the June through October deployment. Monthly means and standard deviations are provided in Table 2. Figure 6a provides daily average AERONET AOT, partitioned into fine and coarse mode components at 532 nm by use of the SDA + algorithm. Average and standard deviation of 532 AOT were 0.17 ± 0.11. Total monthly means were 0.18, 0.16, 0.26, 0.18, and 0.10 for June through October, within 0.01 of pairwise values for clear column lidar averages (Table 2). However, significant variability in AOT was observed owing to pollution and smoke transport episodes. Events greater than the one standard deviation level had AOT values that ranged from 0.28 to 0.55 (e.g., June 25–26, 8–9, 15, 23–24, and 28–30 August, and 7–10 September). Yet daily average AOTs could be below 0.05, often precipitously dropping from the previous day. Fine mode AOT constituted of >90% of total AOT for all but 5 days and never less than two thirds. Those cases with significant coarse mode contribution may have some cirrus contamination. The International Cooperative for Aerosol Prediction multimodel aerosol ensemble [*Sessions et al*., 2015] suggested periodic injections of Saharan dust into the SEUS, but not with appreciable influence at the site.

Daily average and standard deviation of $PM_{2.5}$ at the nearby CSN air quality site (Figure 6b) taken over the study period was 12.0 ± 4.5 $\mu g\,m^{-3}$ or 12.8 ± 4.0 $\mu g\,m^{-3}$ if we consider only those daily average values pairwise with lidar observations (e.g., Table 2). $PM_{2.5}$ events largely coincided with AOTs events listed above (with the most notable event reaching 28 $\mu g\,m^{-3}$ coinciding with 7–10 September 2013) although $PM_{2.5}$ showed much less dynamic range. Consequently, correlations between daily average AOT from AERONET Level 2 data and $PM_{2.5}$ were middling ($r^2 = 0.48$), consistent with the findings of the literature review of *Toth et al*. [2014].

From the UW-HSRL point of view, we can roughly compare the lidar vertical profile with AERONET and $PM_{2.5}$ through comparisons to integrated or layer aerosol backscatter. In Figure 6c we estimated daily average layer AODs that make up the total AOT using the benchmark $S_a = 55$ sr derived in Figure 1 for all 15 min cloud-free cases to a height of 10 km. To give a semiquantitative view of the aerosol structure, layer AODs are provided with altitude ranges based on the overlap point individual. Nominally, we used <1.4 km msl (1.2 km agl) to represent Factor 2, which also roughly corresponded to the average maximum mixed layer height and PBL base state; 1.4 to 2.8 km msl (Factor 1) roughly corresponding to the entrainment zones; 2.8 to 3.7 km (Factor 4) the lower free troposphere and deeper PBLs; and 3.7–4.5 km (Factor 5) representing lower free troposphere, 4.5–5.5 msl (Factor 7) representing to the average 0°C melting level—a common altitude of stability; and finally 4.5–10 km (an aggregation of Factors 3, 6, 8 and 10) representing middle to upper free troposphere. On very rare occasions, such as the example case of biomass burning in section 4.3, smoke was observed above 10 km. For the purposes of this overview time series, the gain of these few days would be offset by significant penalty in additional cirrus contamination. Through inspection, cases of clear smoke in the upper troposphere/tropopause region identified by low depolarizing backscatter above 10 km are signified by a pink mark on Figure 6c. Overall the total average estimated HSRL AOT semiquantitatively match the daily averaged AERONET values (e.g., Figure 1; $r^2 = 0.92$). However, occasional departures did occur. As we discuss in our case studies in section 4, the use of a static lidar ratio tended to overestimate ~20% AOT in cleaner conditions and underestimate AOT ~20% for thick smoke events. This tendency is consistent with the compilation of lidar ratios for different aerosol species by *Burton et al*. [2012].

To identify variability in vertical partitioning, we further fractionalize layer contributions to total integrated aerosol backscatter in Figure 6d. As extinction is linear in S_a, we expect layer uncertainty in light extinction

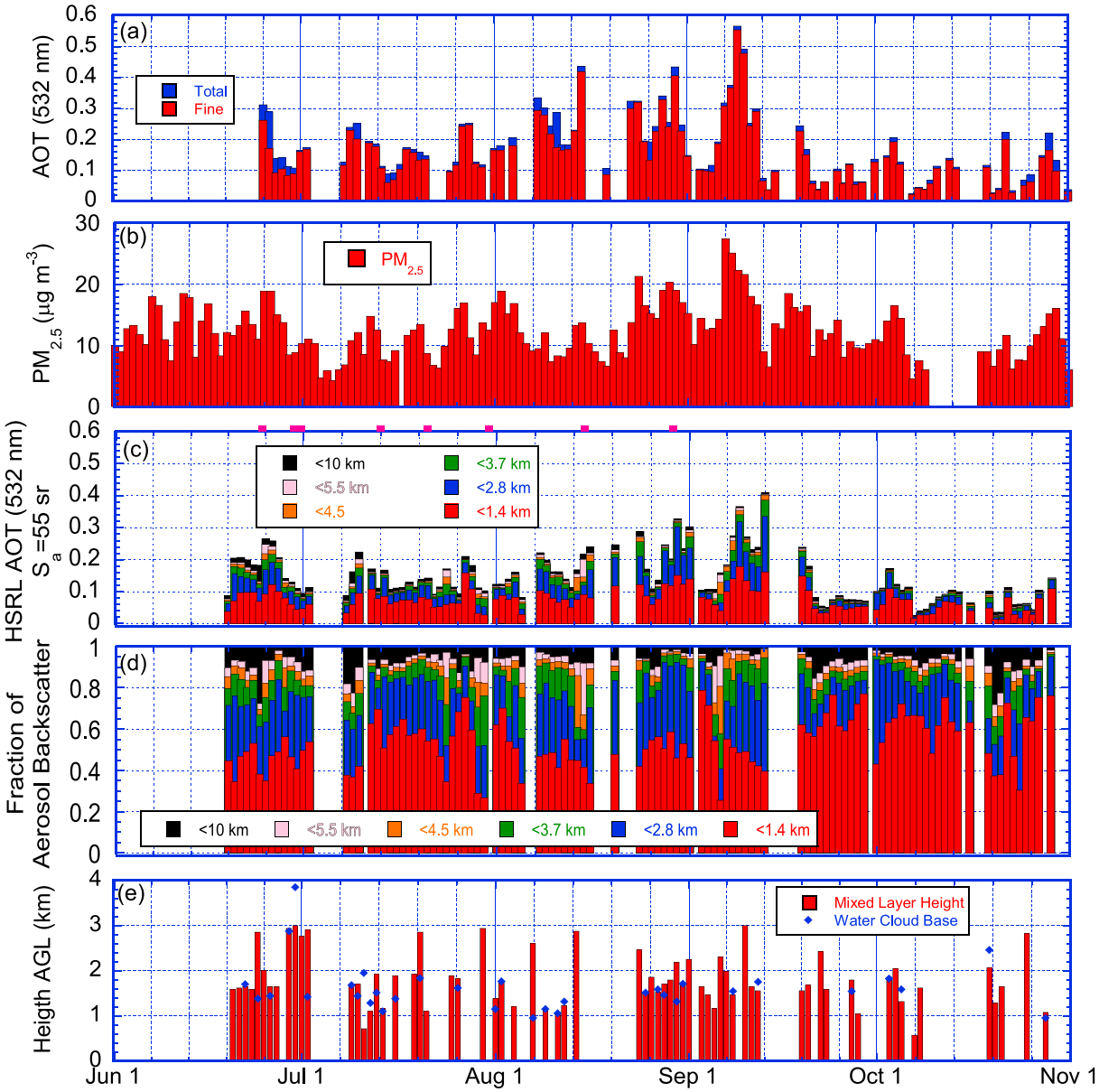

Figure 6. Time series of the Huntsville site for 1 June through 1 November, 2013. (a) Collocated AERONET SDA plus deconvolution of fine and total AOT at 532 nm; (b) Surface $PM_{2.5}$ from the nearby CSN site; (c) Daily average HSRL inferred layer AODs assuming a static lidar ratio (S_a) = 55 str for all cloud-free cases to 10 km. Also, cases of smoke observed the 10 km level are marked in pink; (d) Daily averaged HSRL inferred layer fraction of integrated aerosol backscatter; and (e) HSRL inferred mixed layer height and cloud base from HSRL returns for 18:30 UTC each day.

for individual days to be on par with the comparison of integrated backscatter to AERONET (~18%), not to exceed the realm of possible S_a values (~35%). Extrapolating to the surface for the lowest, ~45–60% of the aerosol backscatter is attributable to <1.4 km msl, or 1.2 km agl. Higher fractions were associated with early fall (e.g., after mid-September). A further 20–30% of integrated backscatter is accounted for in the entrainment zone (~1.2–2.8 km msl), or roughly a total of 70–80% of total integrated backscatter is within typical PBL heights (<2.8 km). Again, generally, there were higher PBL fractions in the early fall. As indicated in the factor analysis, while the most significant contribution to overall AOT is near-surface Factor 2, the variability in AOT was most closely linked to the Factor 1 entrainment zone with larger standard deviations over mean ratios (25–50%). Above the PBL, the lower free troposphere region also on average yielded a ~15% contribution, presumably due to biomass burning transport. A final 6–8% of variance is attributed to 5.5–10 km, with departures as much as 30% for a late June that largely defined

Factor 3 (discussed in section 4.3). Put another way, on average >92% of the total AOT is below 5.5 km, that is, below the 0° C level—again noteworthy for its typical location of more stability.

We can also use the lidar to also help assign individual mixed layer depths. Figure 6e provides mixed layer depth at 18:30 Z (A-train overpass time and typical radiosonde release) based on two methods. First is the HSRL mixed layer height product of *Piironen and Eloranta* [1995] that looks for the first significant maximum in cloud-free aerosol backscatter, similar to many such techniques [e.g., *Cohn and Angevine*, 2000; *Brooks*, 2003]. Second, as a check, water cloud bases are also listed. Under typical environments these bases should be coincident (e.g., CuHu or cumulus mediocris—CuMed) or above (e.g., Ac) the top of the mixed layer. Typically in Figure 6e the two methods are within 200 m of each other. Removing cases of obvious Ac, liquid water cloud base was on average 1.5 km msl (within 100 m of our benchmark). In comparison, the Piiron and Eloranta method on average retrieved 1.6 km, slightly higher. This mismatch is due to several phenomena. First, we have already seen in Figure 5 how there is aerosol backscatter enhancement below clouds and suppressed backscatter between clouds. Necessarily then, for cloud-free profiles there is likely drier air, and hence, the mixed layer can continue to grow below saturation. If there is an aerosol layer aloft (such as detrainment layers at the top of the entrainment zone), a maximum aerosol backscatter or liquid cloud base will also bias the result. Finally, in very complex cases of free tropospheric aerosol transport just above there PBL, aerosol backscatter algorithms can key in on the wrong peak in aerosol backscatter.

Based on the time series of Figure 6 coupled with the examples in Figures 3 and 6, the SSEC HSRL deployment provided a unique data set for understanding the dynamics of aerosol particles and clouds in the SEUS. Multiple studies are underway to quantitatively mine these data products for air quality, free tropospheric boundary layer dynamics, pyroconvection, etc. In the following section, specific examples of dominant aerosol behaviors to supplement our fair weather case are provided to help interpret the lidar time series data.

4. Results and Discussion: Case Examples of Aerosol Layering Phenomenon

In section 3 we provided an overview and time series of basic aerosol characteristics as derived from the UW HSRL. Included was a brief description of a "typical" baseline fair weather day of a mix of a polluted PBL with biomass burning smoke aloft. However, as observed in Figure 6, there is significant variability in aerosol vertical distribution over the study period. In this combined results and discussion section, we present three aerosol events that represent modes of variability that largely modulate this aerosol vertical structure at the site. These include section 4.1: Strong convective regime which decouples $PM_{2.5}$ and AOT; section 4.2: A classic early autumn frontal passage that clears a boundary layer air pollution event to explain dramatic decreases in AOT; and section 4.3: A complex free tropospheric biomass burning smoke phenomenon, including convective injection to the top of troposphere by mesoscale convective systems that created significant spikes in AOT.

4.1. Aerosol and Cloud Layering Near Convection, 8 August 2013

From the installation of the UW HSRL in mid-June, through the middle of September, the SEUS was in a typical summer time phase with periods of convective activity (e.g., see *Toon et al*. [2016] for an overview). The fair weather day of 27 August 2013 presented in section 3.2 can be then contrasted with a canonical case convective enhancement as CBs passed through the area. Often convective enhancement was a result of a combination of Gulf of Mexico moisture being advected northward into the region, with instability provided by occasional weak cold fronts or waves propagating around the western monsoon from the northwest. This led to a removal of the large-scale subsidence inversion (e.g, at 2.5 km in the 27 August case), deeper convective clouds, and loose lines of diurnally varying CBs often adverting southeastward through Tennessee to the Huntsville area. Occasionally, these CBs could be severe, with the local weather service noting up to 4 cm of precipitation in the course of a few hours.

Here we examine 8 August 2013 as representative of several sets of aerosol and cloud profiles in the vicinity of deep convection. That is, how a fair weather aerosol vertical distribution compares to a more convectively active period. For 8 August model and trajectory analyses reject that western biomass burning smoke had influence in the region. Thus, we can surmise that this event demonstrates vertical redistribution of regional PBL aerosol particles into the lower free troposphere and perhaps aqueous phase production of aerosol mass

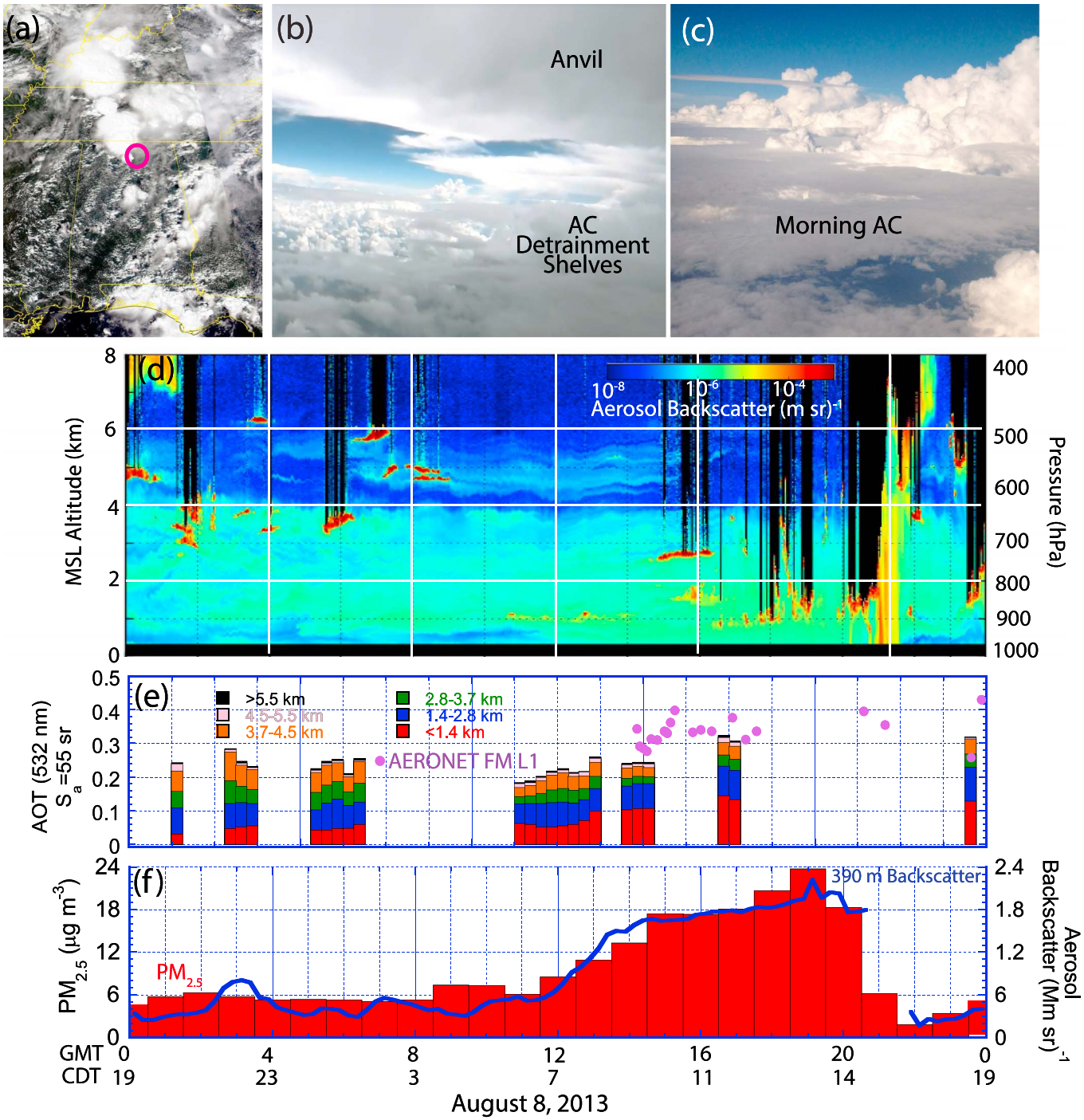

Figure 7. (a) Regional Aqua MODIS RGB for 8 August 2013 13:30 UTC. (b and c) Example altocumulus cloud pictures taken during SEAC^{4}RS showing formation from deep convection and mediocris, respectively. (d) The 532 nm aerosol backscatter time-height plot of 8 August 2013 in a convective regime. (e) Corresponding hourly average 532 nm layer HSRL inferred AODs and AERONET fine mode AOTs. (f) Corresponding CSN site $PM_{2.5}$ and 532 nm HSRL 390 m msl aerosol backscatter.

[*Su et al.*, 2008; *Jiménez-Escalona and Peralta*, 2010; *Wonaschuetz et al.*, 2012; *Eck et al.*, 2014; *Wagner et al.*, 2015]. Other cases that have aircraft data are a topic of a subsequent paper.

The Aqua MODIS RGB image for 8 August is provided in Figure 7a, showing an area of thunderstorms that developed in Tennessee and began propagating to Huntsville (marked as a circle). For context, included are SEAC^{4}RS mission photos of cloud environments of more active convective phases, including an

afternoon photo from Alabama on 12 August 2013 showing a series of altocumulus (Ac) shelves forming between the thunderstorm anvil above, and cumulus clouds below (Figure 7b), and another series of Ac clouds photographed on 11 September 2013 in eastern Texas that formed in the morning hours in a field of Cu to Cumulous Congestus-TCu (Figure 7c). In all of these images, we see complicated field of convective and altocumulus clouds of various heights. Day 8 August 2013 provides an excellent example of how aerosol particles are distributed in these convectively enhanced environments.

A time series of aerosol backscatter for 8 August is presented in Figure 7d up to an altitude of 8 km to add detail for the middle free troposphere. As in Figure 6, altitude AOD components to the total AOT are presented using an $S_a = 55$ sr in Figure 7e with our representative levels of <1.4 km, 1.4–2.7 km, 2.7–3.7 km, 3.7–4.5, 4.5–5 km, and 5.5–10 km. Included are 532 nm AERONET fine mode AOTs processed with the SDA plus algorithm using level 1 data (level 1.5 or 2 data were unavailable due to thin cirrus of COD = ~0.03). The HSRL and AERONET AOTs generally matched, with the HSRL's assumed lidar ratio of 55 sr being perhaps ~20% low. Hourly surface $PM_{2.5}$ from the CSN air quality station with 390 m backscatter is given in Figure 7f.

Before the start of the time series, one precipitation cell passed through the area at ~22:00 Z 7 August, reducing near-surface $PM_{2.5}$ concentrations from 16 to 1 $\mu g\ m^{-3}$ in 1 h. $PM_{2.5}$ quickly increased to 6 $\mu g\ m^{-3}$, the start of the time series in Figure 7 (0Z UTC or 19:00 CDT just as the Sun has set). We consider that this a suitable starting time of a diurnal cycle in a convectively active environment. At sunset, estimated 532 nm AOTs were on the order of 0.25. This is near to the daily average for our base case of 27 August. However, unlike the 27th, the HSRL suggests that only ~15–20% or aerosol backscatter is within the lowest 1.4 km. Instead, the remaining aerosol backscatter is largely equally partitioned in the 1.4–2.8 km, 2.8–3.7 km, and 3.7–4.5 km altitude ranges. That is, $>80\%$ of the total AOT is likely between 1.4 km and 4.5 km. Clearly visible in the nighttime hours is a nocturnal boundary layer, roughly 500 m in depth. $PM_{2.5}$ and aerosol backscatter values were roughly constant during nighttime hours. Also, relatively constant during the example period is a sharp delineation in aerosol backscatter at ~4 km. Notably, the radiosonde placed the 0°C level at 4.2 km. As previously mentioned this level is a common level of enhanced stability in convective environments. For the fair weather case of 27 August, the regional subsidence inversion at ~2.5 km msl capped PBL development. In a similar way, we speculate that the 0°C and its tendency to cap CuMed and small TCu clouds acts similarly, making a functionally deep entrainment zone. Between the surface layer and the 0°C level, we see more variability in aerosol layering structure in both the vertical and horizontal dimensions. Clearly in this laminar free tropospheric regime, intrusions of aerosol particles injected aloft are being observed as they advect over the site.

A second interesting component in this scene is the high prevalence of Ac clouds, both above and below the 4.2 km 0°C level. These types of clouds are exemplified in those types in Figures 7b and 7c, respectively. Notably, Ac in the 4 to 6 km regime bears strong consistencies to detrainment shelves from CBs (Figure 7b). The exact origin of these shelves has not been actively studied, but they can be reproduced in cloud resolving models [e.g., *Posselt et al*. 2008]. Current thinking is that they are related to the formation of inversions as snow and graupel melt once they fall below 0°C. These inversions formed from falling and melting ice then reduce detrainment from water and clouds in the updraft. Again, for this particular case, the melting level is at 4.2 km and many warm Ac clouds are within 1°C of this temperature. Interestingly, these Ac clouds are all clearly embedded in clear aerosol layers. Additional Ac clouds also appear at 5 to 6 km, corresponding to temperatures of -4 to -10°C. HSRL depolarization data suggest that these clouds remain in liquid phase. So the causal mechanism may be due to cloud top detrainment from TCu rather than CB detrainment shelves. Interestingly, aerosol returns associated with these colder clouds are an order of magnitude less than their 0°C counterparts. This may be indicative of the amount of PBL air being detrained into the free troposphere by these different cloud types.

Also in the very early morning hours are Ac clouds forming well below 0°C. This case is exemplified by Figure 7c, e.g., visible in the 2.5 to 3 km altitude range, such as at 16:00 UTC. These Ac are not a result of detrainment from deep convection but, as discussed in section 3.1, a result of moisture enhancement due cloud top detrainment from Cu. A layer of aerosol backscatter also accompanies these clouds.

A clear transition from nighttime to daytime boundary layer structure is also visible in Figure 7c, with a developing boundary layer cloud structure initiating at 9:00 CDT similar to that of the base case of 27 August. However, cloud returns and GOES cloud height (not shown), suggest by early afternoon boundary layer clouds, are much deeper than their 27 August counterparts—up to the 0°C level. Also, in the morning and

afternoon of 8 August, $PM_{2.5}$ concentrations grew by a factor of 4 from 6 to 24 $\mu g\ m^{-3}$. Aerosol backscatter grew likewise. AOT, however, grew by only by 25–50%, reaching a maximum of ~0.35. Then as the next precipitating cell moved over Huntsville occurred at 22 Z 8 August, surface $PM_{2.5}$ dropped to 1–2 $\mu g\ m^{-3}$. $PM_{2.5}$ climbed back to 5 $\mu g\ m^{-3}$ by sunset 3 h later. We have a vertical profile not unlike the start of the time series, clean at the surface with an optically thick aerosol layer to the 0°C level. Likewise, the cycle repeated the following day. For reference, readers can review a replot to this time series over this period at the UW HSRL site at http://hsrl.ssec.wisc.edu/, last accessed on 23 November 2016.

The 8 August time series is interesting at a number of levels. First, these convective precipitation events rapidly reduce particle mass and extinction loadings at the surface yet are followed by a rapid recovery, notably in daylight hours. This may be due to emissions, secondary particle production, or simply transport from areas not experiencing precipitation. For 8 August, significant AOTs of 0.3–0.4 existed poststorm despite the clean surface conditions and 72 h back trajectories local to the SEUS. Thus, these layers are likely an indicator of significant detrainment or mixing around the storm by an apron of cumulus clouds. Regardless, AOT and surface $PM_{2.5}$ are largely decoupled. The 8 August HSRL data also pose interesting questions related to the lifecycle and cloud impacts of aerosol particles in convective regimes. Clearly in poststorm environments the aerosol layering structure becomes complex, with significant detrainment of aerosol particles into the lower free troposphere, dominating column AOT—even outside the more traditionally explanation of cloud halos. Finally, Figure 7 also highlights a largely unstudied field of aerosol particles as nuclei for and from Ac. Ac clouds are prevalent [*Heymsfield*, 1993; *Parungo et al*., 1994; *Sassen and Wang*, 2012], accounting for 20–40% reports of clouds, but receive very little attention in the scientific community [*Gedzelman*, 1988]. Past studies that have been done have focused on particles as ice nuclei, leading to glaciation in supercooled Ac clouds [e.g., *Sassen and Khvorostyanov*, 2008; *Ansmann et al*., 2009]. However, warm Ac should be given more attention. Over 20 years ago *Parungo et al*. [1994] found that surface reports of clouds indicated an increase in midlevel cloudiness perhaps, they speculate, due to increased levels of aerosol particles. Based on the observations at Huntsville, clearly, there are aerosol layers associated with warm Ac formation, with significant differences above and below the 0°C height. Thus, we believe Parungo et al.'s long standing hypothesis is a valid one and also the topic of a subsequent paper.

4.2. Simple Frontal Passage 19–22 September 2013

The 8 and 27 August example days qualitatively represented much of the June through mid-September deployment. However, by mid-September until operations ceased in early November, temperatures dropped and weather patterns shifted to a more fall-like frontal activity. With cooler temperatures, biogenic emissions significantly reduced, likewise reducing regional aerosol loadings during the SEAC^{4}RS mission [*Toon et al*., 2016]. The end of the burning season in the west also reduced the frequency of midtropospheric aerosol layers (e.g., Figure 6). Finally, a reduction in convection and reduced frequency and height of PBL clouds resulted in a 20–30% fractional increase in column AOT being attributed to the lowest 1.4 km.

From a dynamics, aerosol chemistry, and data continuity perspective, the frontal passage of 20 September 2013 demonstrates the transition of the aerosol environment from the summertime to fall regimes. A set of figures describing this event is presented in Figure 8. Included are MODIS Aqua RGB images for 19 and 21 September 2013, in Figures 8a and 8b, respectively, showing prefrontal and frontal passage. Corresponding 925 hPa winds (or ~725 m msl, or 525 m agl) representing mid mixed layer from the ECMWF reanalysis are provided in Figures 8c and 8d, respectively. Aerosol variability is presented in Figure 8e for the 19 September, 18 Z to 22, 18 Z period as an aerosol backscatter time-height cross section from to 5 km msl altitude. Notable is precipitation from frontal passage on 20 September, 0 to 15 Z. Layer AOD contributions to AOT and AERONET SDA plus processed 532 nm AOT for the example period are also shown with integrated aerosol backscatter from the HSRL for cloud-free cases scaled to an inferred AOT using our baseline S_a of 55 sr (Figure 8f). In general, the HSRL inferred and AERONET AOTs matched, with the HSRL lidar ratio of 55 sr being perhaps 15% too high for the later periods. To characterize surface $PM_{2.5}$ and light extinction, the CSN $PM_{2.5}$ monitoring site along with aerosol backscatter for a 90 m average 390 m msl (190 m agl) high bin is provided in Figure 8g.

In the lead up to frontal passage on the afternoon of 19 September, the region was under the influence of a strong high-pressure system centered over Alabama with an associated inversion at ~2 km msl. PBL and

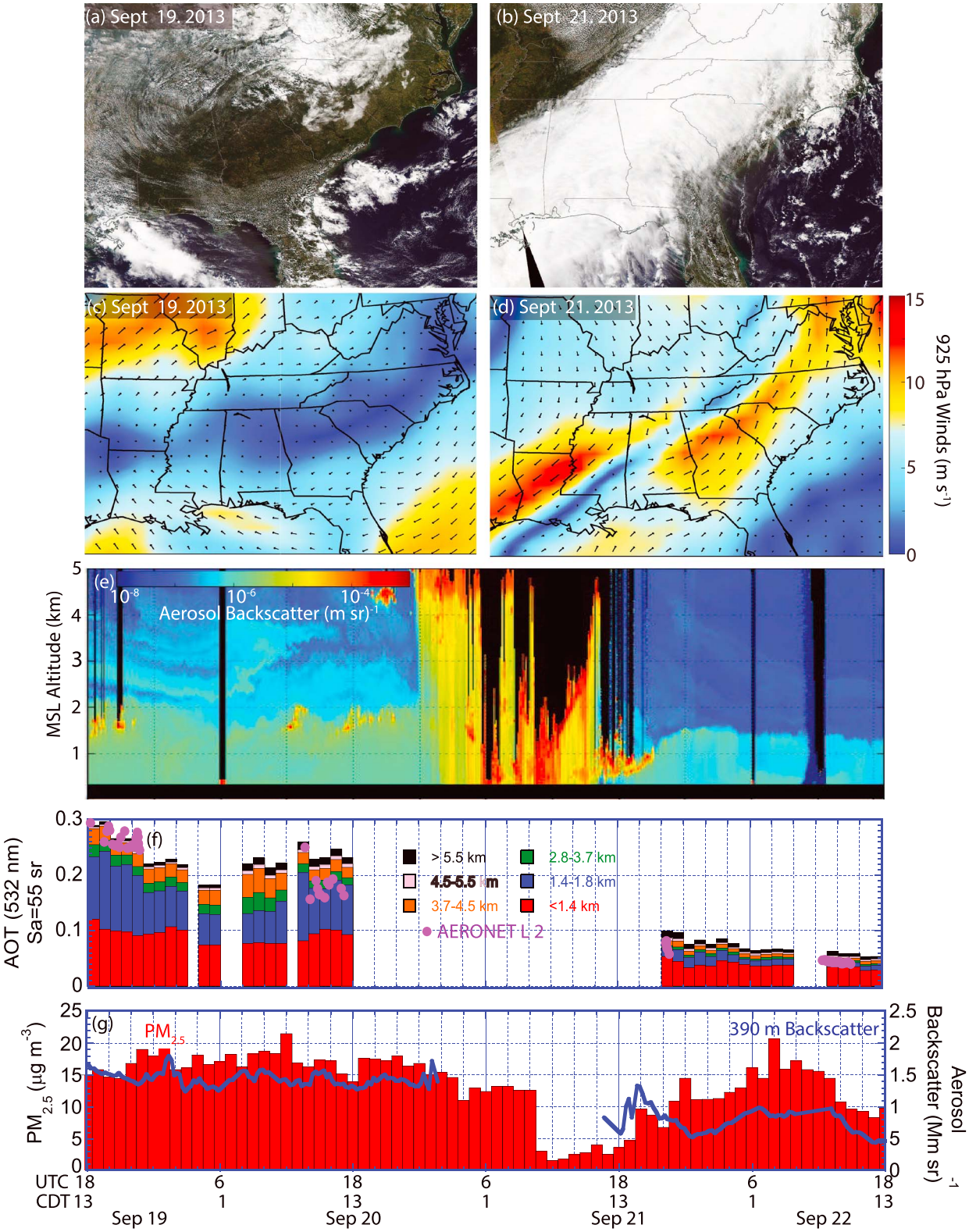

Figure 8. Time series data of a frontal passage at the Huntsville lidar site over the period of 19 September 18 Z through 22 September 18 Z. Included are (a and b) Aqua MODIS RGB images for 18 Z on 19 September at the peak of AOT over the past week followed by 21 September 18 Z just as the front was passing Huntsville. (c and d) ECMWF reanalysis 925 hPa winds corresponding to the MODIS images in Figures 8a and 8b, respectively. (e) UW-HSRL time series for aerosol backscatter; (f) AERONET-derived 532 nm total and fine AOT with HSRL inferred AOT for cases of cloud-free columns to 10 km and an assumed lidar ratio of 55 sr. (g) Hourly $PM_{2.5}$ data from the CSN air quality site with HSRL aerosol backscatter at 390 m msl, or ~190 m agl.

lower free tropospheric winds across the entire SEUS were light (2–5 m s^{-1}, e.g., Figure 8c). This situation is not unlike the initial example of 27 August 2013 used in Figures 3–5, with some additional enhancement in the entrainment zone as described in section 4.1. Thus, a detailed description is not repeated here. In the afternoon of 19 September, there were scattered CuHu with cloud bases detected at ~1.7 to 2 km msl. AOT at 532 nm peaked at 0.28 and $PM_{2.5}$ at 21 μg m^{-3}. UW-HSRL scaled AOT using $S_a = 55$ sr yielded an AOT on par with AERONET. The surface to the subsidence inversion (functionally the midday PBL height) accounted for >75% of integrated aerosol backscatter (or nominally AOT). The remaining AOT was accounted for below the 4.3 km/0°C level with trajectories suggesting likely origins of agricultural burning and pollution from the Mississippi Valley. By the next day (20 September 18 Z), the high had moved into Georgia and Northern Florida, and a cold front started its descent into the SEUS, bringing with it southwesterly winds to ~7 m s^{-1} and 10 m s^{-1} at 925 hPa and 700 hPa, respectively. These winds ventilated Alabama with southern Mississippi and Gulf of Mexico air.

The UW HSRL detected virga and light rain at the Huntsville site at 21 September ~3 Z. Accompanying these rain showers were only slight decreases in $PM_{2.5}$. The period of heavy rain began at 21 September ~10 Z and continued for 3 h. At this point hourly $PM_{2.5}$ dropped to its lowest level during the deployment, 1.5 μg m^{-3}. Over the next several days after frontal passage the region experienced clear skies (Figure 8b), northwesterly winds (Figure 8d), and low AOTs (Figure 7f). AERONET 532 nm AOT values reached a minimum as low as 0.035 by 22 September. Above the mixed layer, air was exceptionally clean, with free tropospheric extinction of ~0.001–0.003 km^{-1} for $S_a = 55$ sr, compared to Rayleigh scattering coefficient of 0.01 km^{-1}. Even so, some light aerosol features are nevertheless visible in the aerosol backscatter signal. The postfrontal daytime mixed layer was shallow, 0.5–1.2 km deep. A ~300 m deep nocturnal surface layer is also visible in the morning hours of 21 September. Interestingly, unlike AOT, $PM_{2.5}$ began to recover immediately after the precipitation event. In fact, when AOTs were at 0.05 at 22 September 13 Z, $PM_{2.5}$ was at 15 μg m^{-3} —equal or above monthly average values.

The above narrative nicely depicts aerosol dynamics in contrast to the convective regimes described earlier. The passing front not only locally cleaned the PBL but associated wind shifts also advected a large cleaner free tropospheric air mass with it. The decoupling of surface $PM_{2.5}$ from AOT is also clear owing to surface layer dynamics. Thus, while long period climatologically analyses report some large-scale covariance between AOT and $PM_{2.5}$, [e.g., *Wang and Christopher*, 2003 to most recently *Chu et al.*, 2015], this frontal case exemplifies the common observability limit of r^2 of ~0.5 seen in correlation studies. This case also demonstrates the conclusions of *Toth et al.* [2014] that even using lidar backscatter data at altitudes to 400 m is still sometimes insufficient to improve surface monitoring.

4.3. Free Troposphere Biomass Burning Layers on 23–25 June 2013

Severe drought conditions in 2013 led to an extensive 2013 biomass burning season in the western United States. In June, significant burning activity occurred in Colorado and New Mexico, with fire activity shifting to California and the Pacific Northwest from late July to August (e.g., National Interagency Fire Center reports, https://www.nifc.gov/ and http://inciweb.nwcg.gov/). Free tropospheric aerosol layers were observed at the Huntsville site on most days in June through mid-September with indications from the trajectory analysis that they largely were of biomass burning origin. As discussed in section 3 and *Toon et al.* [2016], the impact of fires on AOT over CONUS was quite visible in monthly MODIS AOT values, particularly August. While a more comprehensive study of biomass burning vertical characteristics and sources is outside of scope here, an example is given of the most dramatic biomass burning event observed during the UW HSRL deployment that demonstrated the multifaceted behavior of such plumes.

The most significant biomass burning event observed at Huntsville occurred just after the start of operations, over the 24 to 25 June period with significant smoke advection into the SEUS at multiple levels up to 14 km. In fact, based on the regional AERONET deployment, this event resulted in the largest AOT spike over the entirety of the SEUS for all of 2013. Our analysis suggests that the origins lay in severe wildfires in Colorado, namely, the 7000 ha Black Forest fire south of Denver CO (latitude = 39.0, longitude = −104.8) and the 7000 ha West Fork Complex in the southern Rocky Mountains (latitude = 37.5; longitude = −106.9). With high aerosol loadings to 14 km, we originally suspected pyroconvection as a contributor to this event [e.g., *Fromm and Servranckx*, 2003; *Fromm et al.*, 2010]. However, as discussed below, we now believe that this event was a result of smoke

interacting with mesoscale convective systems (MCSs) in a manner similar to the many cases of smoke being vertically transported throughout the tropospheric as analyzed in *Guan et al*. [2010].

Contextual information on regional biomass burning smoke activity is provided in Figure 9, with aerosol backscatter and total depolarization information at Huntsville showing smoke to >13 km altitude being presented in Figure 10. The roots of this event occurred the night of 21 June, with global multispecies aerosol models [e.g., *Sessions et al*., 2015] and the Navy Aerosol Analysis and Prediction System reanalysis [*Lynch et al*., 2016] forecasted smoke from multiple fires in Colorado being transported up into an MCS forming that night over Nebraska. At that point, the forecast global models failed to forecast smoke properly as they are not equipped to cope with a deep convective transport. However, we can see the result of this interaction in OMI OMAERUV-UV aerosol index level 3 products for 22 and 23 June in Figures 9a and 9b, respectively. As discussed in *Guan et al*. [2010], aerosol index values in the 6–10 range are solid indicators of optically thick smoke in the upper troposphere. Also shown in Figures 9c and 9d are area boxes corresponding to 22 June Terra MODIS and 23 June Aqua MODIS RGB images, respectively (Terra is used in Figure 9c due to better coverage). Clearly visible in the 22 June image is a region of darkened cirrus clouds in northern Nebraska and southern South Dakota behind an MCS, corresponding to aerosol index values of 8–10 in the OMI product. Also across the Nebraska to Kansas, a thinner belt of darkened cirrus and high aerosol index on the order of 9–10 also exists. These values are consistent with the values found in *Guan et al*. [2010], owing to the presence of smoke at high altitude in highly reflective cirrus. All of these factors indeed enhance aerosol index [*Torres et al*., 2007]. Interestingly, the region of these hotspots also corresponds well to the map of like events in *Guan et al*. [2010] as a region of frequent smoke-MCS interaction. These events were very far reaching and serendipitously captured by a CALIPSO overpass at 23 June ~8:25 UTC whose track went along the east coast of Texas, though Missouri and over the Lake Superior (track over the corresponding Aqua MODIS 11 μm brightness temperature in Figure 9e). Corresponding CALIOP aerosol backscatter and depolarization curtains are subsequently shown in Figures 9f and 9g, respectively. Cleary evident in Figure 9f is a midlevel tropospheric aerosol layer from 32 to 39°N latitude at 4 to 6 km above a polluted PBL. Other strong but vertically limited smoke features are also visible from 38 to 42°N including one layer at 14 km and several from 6 to 10 km. These plumes slightly depolarized the lidar beam on the order of ~10%. At this point CALIPSO crossed directly over another MCS system, exiting over Lake Superior. North of the MCS lidar attenuated backscatter showed very strong returns from 48 top 53°N latitudes ranging from 8 to 13 km. This feature, as well as the upper tropospheric 40°N layer, was classified as cirrus cloud in the CALIOP V3.3 vertical feature mask. However, examination of this feature in light of associated depolarization data, and inference from OMI aerosol index the afternoon after (e.g., Figure 9b), suggests that it is, in fact, detrainment from a second MCS with embedded cirrus at 10 km altitude. Between OMI and CALIOP, clearly the middle to late June timeframe was a remarkably active period of smoke convection interaction. Indeed, on subsequent days, this event was visible in OMI as far as Scandinavia and perhaps detected in eastern Europe [*Markowicz et al*., 2016].

The UW HSRL captured the June continental scale smoke event with great clarity. Figure 10a presents the 23–25 June 2013 time-height cross section of aerosol backscatter to 15 km, demonstrating exceptional aerosol structure throughout the free troposphere. This one case is largely responsible for several of the upper free tropospheric factors in Figure 1c, including Factor 3. To distinguish smoke from cirrus clouds, backscatter depolarization is presented in Figure 10b, with cirrus being clearly identifiable with depolarization higher than 20% and typically on the order of 40%. In some particularly clean areas, anomalous enhancement in depolarization is visible due to signal-to-noise limitations (e.g., 9 km at 23 June, 6–12 Z).

Within the time period of Figure 10a, layering structure is seen in the free troposphere with plumes ranging from just above the PBL (2–3 km), to a significant plume at 11 to 13 km. While the AERONET site did not come online until 25 June 2013, simplified AOT contributions using the baseline $S_a = 55$ sr are provided in Figure 10c, including a new range gate from 10 to 15 km. HSRL estimates are that column AOTs may have reached 0.5, with the 11–13 km plume causing the 10–15 km layer AOD to increase to 0.25, accounting for half of the total AOT. The following day, middle free tropospheric smoke layer AOD enhancements to the column were on the order of 0.1 to 0.15. However, smoke commonly has lidar ratios on the order of 70 [e.g., *Burton et al*., 2012]. Thus, these HSRL estimates of smoke contributions to total AOT are likely low biased, perhaps as much as 30%.

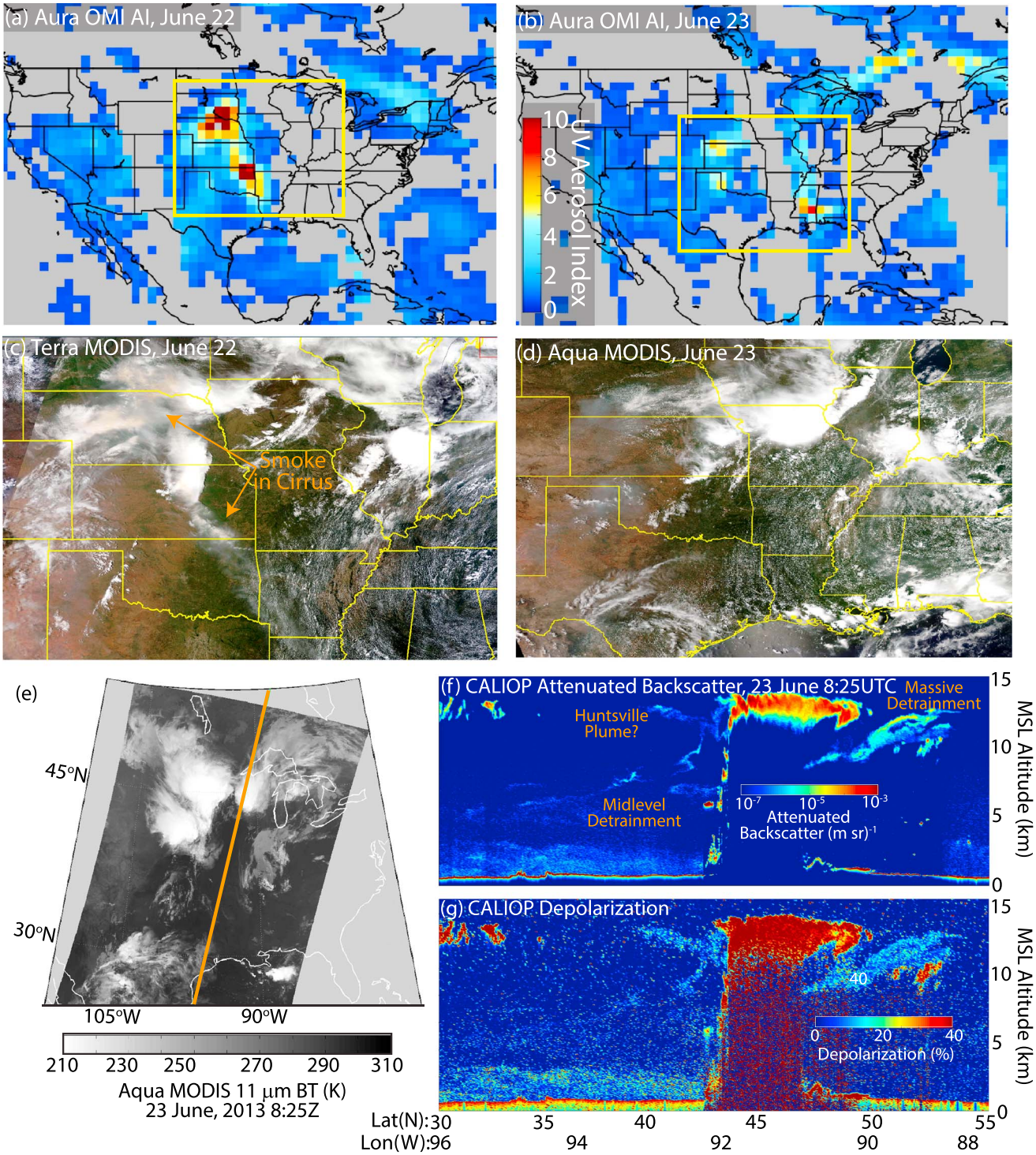

Figure 9. OMI, MODIS, and CALIOP views the regional biomass burning environment leading to the 24–25 June smoke events at Huntsville. (a and b) OMI UV aerosol index (*AI*) for the afternoon of 22 and 23 June, respectively, showing high values (>5) of locations where smoke has been lofted to the upper troposphere. Marked in yellow are boxes of the regions for Figures 9b and 9c of Terra MODIS RGB image for 22 and 23 June showing smoke ingested in a convective systems. Visible are two major smoke features, including significant darkening of cirrus by intermingled smoke in northern Nebraska and South Dakota and a leader of smoke in southern Kansas into Oklahoma, also with embedded cirrus. For 23 June showing the movement of convection into Missouri and Illinois with smoke also visible from the southern leader in the Mississippi Valley. (e) CALIPSO track over the region for 23 June 8:20–8:25 UTC (e.g., between the 22nd and 23rd) over MODIS Aqua Channel 31 (11 μm); with (f and g) corresponding CALIOP 532 nm attenuated backscatter and depolarization. Note, in southern latitudes, (e.g., 35–40°), filaments of some are visible, including a 5 and 13 km plume which we suspect is associated with the Huntsville observation. Also visible in this data is a massive upper level smoke detrainment event in the 10–13 km range, suspected to be associated with the smoke over northern Nebraska visible in Figure 9a.

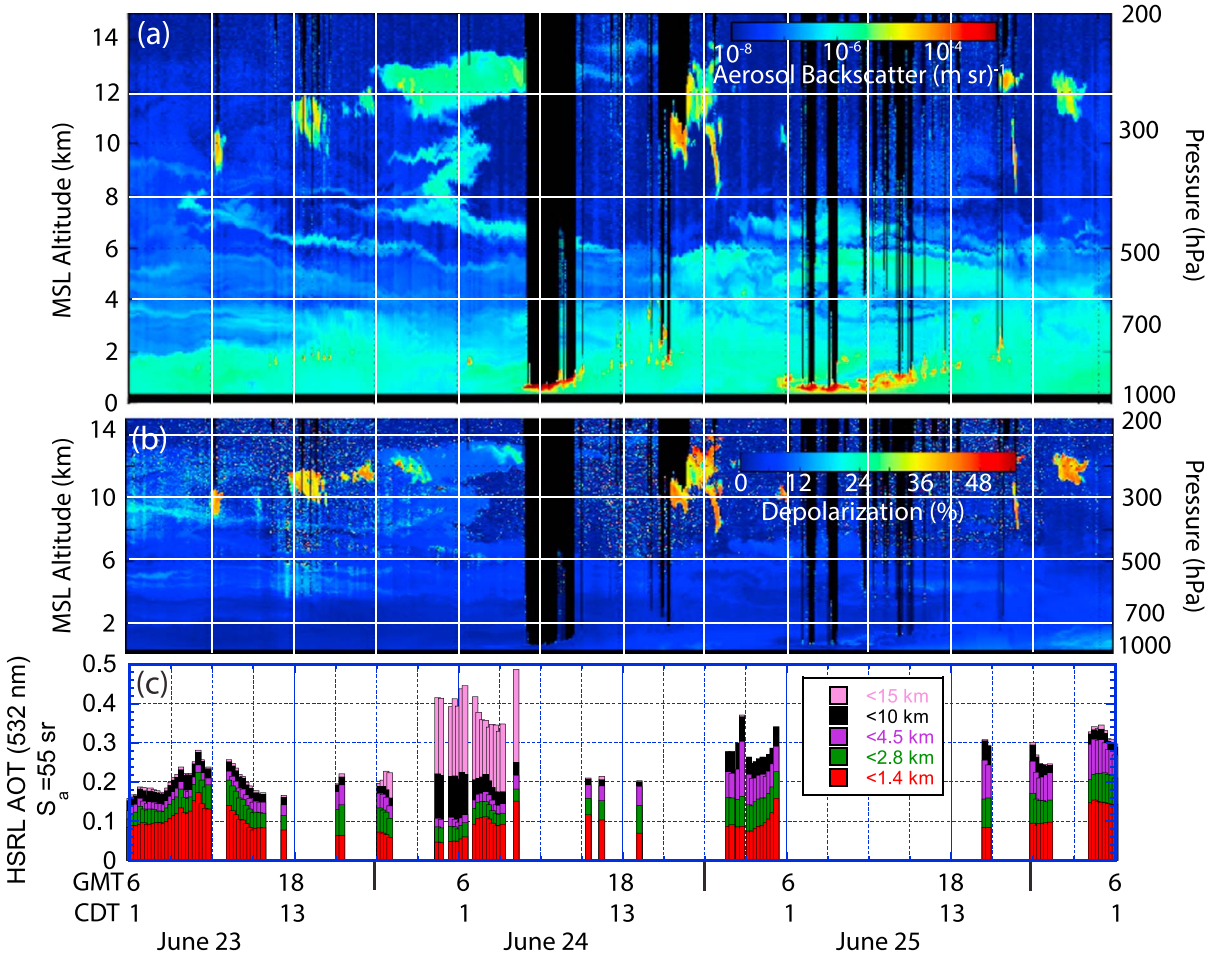

Figure 10. Time series of the most significant biomass burning event to reach the Huntsville lidar site. Included are HSRL (a) aerosol backscatter, (b) depolarization, and (c) incremental inferred aerosol optical depth assuming a baseline lidar ratio (S_a) of 55 sr.

Finer atmospheric vertical structure for these events is presented in Figure 11, including 2 h-averaged (a) aerosol backscatter and (b) depolarization for three largely cloud-free periods, 24 June 2013, 6:00 UTC corresponding to the peak of the 11–13 km layer; 25 June 2013, 18:00 UTC corresponding to the mid tropospheric event; and 24 June 2013, 12:00 Z as an intermediate period. While SEACONs radiosondes would not be deployed for another 40 days, the Birmingham radiosonde site 150 km to the south is available. However, the 11–13 km plume event fits between the 0:00 and 12:00 UTC releases, and by 26 June 23 0:00 UTC, the event was largely over. Despite these timing and location differences, the radiosonde observations provide some insight into tropospheric vertical structure at the synoptic level.

Considering first the free tropospheric aerosol event from 24 June 0 to 12 Z, strong aerosol backscatter was observed from 6 to 13 km in two key layer objects above a typical polluted PBL. The first layer, from 6 to 10 km, has a backscatter of ~5×10^{-7} (m sr)$^{-1}$ corresponding to a nominal 532 nm extinction of 0.03 km^{-1} and layer AOD of ~0.12. Notable in this layer is a lightly elevated depolarization ratio of 8–10%, versus 2–3% in the PBL below. Such slight depolarization has been noted in smoke plumes before [*Burton et al.*, 2012] and is consistent with the CALIOP depolarization of smoke in Figure 9e. At the topmost level, the 11–13 km plume of backscatter is up against the base of the tropopause inversion from the temperature and virtual potential temperature plots of Figures 11c and 11d. Even after this core event has ended, some traces of layers near the tropopause are visible until 26 June 2013 0 Z, even as high as 14.5 km, well within the inversion.

HSRL depolarization also provides some insight into aerosol characteristics. Overall in the plume aerosol depolarization is at ~12%, slightly higher than the smoke in lower levels. Interestingly, from Figure 10b, embedded within this upper level plume (~1:00 and 10:00 UTC) are two areas of highlighted

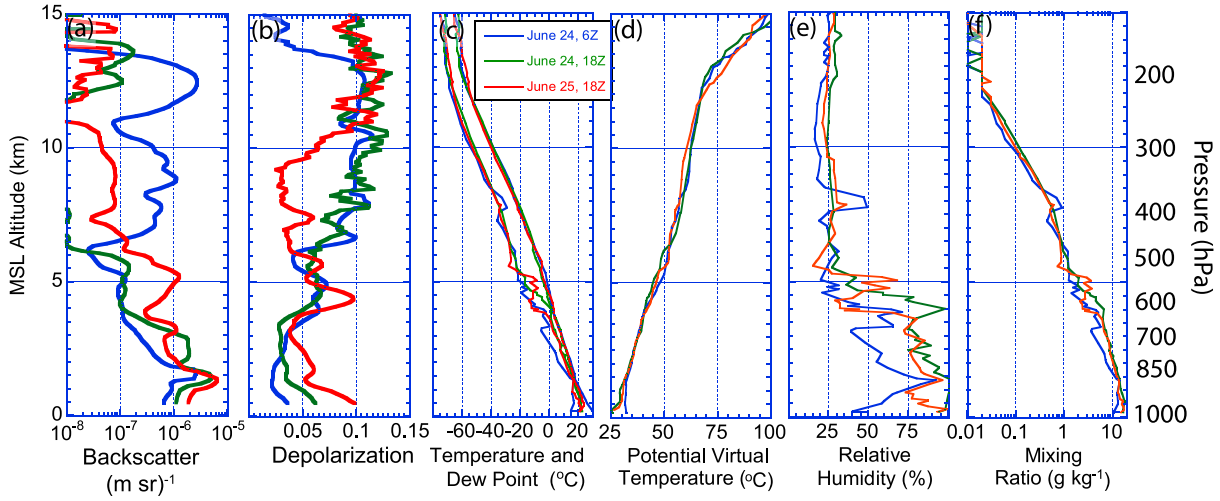

Figure 11. (a and b) Aerosol backscatter and depolarization from the Huntsville HSRL capturing the vertical profile of biomass burning smoke in the free troposphere. Included is corresponding sounding data from the Birmingham radiosonde station 150 km to the south of Huntsville for (c) temperature and dew point, (d) potential virtual temperature, (e) relative humidity, and (f) mixing ratio.

depolarization indicative of cirrus, with values on the order of 25–50%. The characteristics of these clouds are consistent with tropopause transition layer cirrus in the vicinity of deep convection [e.g., *Winker and Trepte*, 1998; *Garrett et al.*, 2004; *Fueglistaler et al.*, 2009]. Other cirrus clouds in the scene are at lower altitudes (~10–12 km) and have higher depolarizations of nearly up to 50%. But even for the same altitude, clearly the cirrus within the smoke plume has a lower depolarization ratio, perhaps related to aerosol effects.

A second event was advected over the site over the entirety of 25 June 2013. In this case, two individual layers are visible as well, from 4 to 6 km and a smaller secondary plume from 6 to 7 km. These plumes are also slightly depolarizing. Comparing these aerosol backscatter profiles with the soundings from Birmingham, the aerosol layers were in association with notably, the 0°C midlatitude inversion serving as a boundary.

Figures 10 and 11 demonstrate that optically significant biomass burning layers could appear anywhere in the free troposphere with fine structure in vertical extent on the order of hundreds of meters. Also from Figure 6 there was a proclivity for these layers to be separated by the ~ 4.5 km/ 0°C level over the course of the deployment (note the separation of plumes right at ~4.2 km). In general, for smaller and moderate events, this level of stability is consistent with plume rise observations. For example, *Val Martin et al.* [2010] saw a mean of plume rise values for North American biomass burning at 4.2 km. While they recognized this altitude of stability, they did not recognize the special significance that this level corresponds to ~0°C. Even so although smoke plumes tended to be near or below the 0°C line, particularly strong plumes or plumes interacting with deep convection can clearly penetrate the upper free troposphere or even reach altitudes well within the tropopause. Based on visual inspection of data (as shown in Figure 6 and visible on the UW HSRL website), smoke was found above 10 km on seven occasions, including the example shown here. In particular, 8–10 July, 28–30 July, and 14–16 August are equally dramatic in their complex layering structure through the troposphere.

5. Summary and Conclusions

The purpose of this paper is to provide an overview of the deployment of the University of Wisconsin 532 nm wavelength High Spectral Resolution Lidar (UW-HSRL) to the University of Alabama Huntsville (UAH) National Space Sciences Technology Center (NSSTC) Regional Atmospheric Profiling Center for Discovery (RAPCD) lidar facility from 19 June to 4 November 2013. This deployment, sponsored by the NASA Cloud-Aerosol Lidar and Infrared Pathfinder Satellite Observations (CALIPSO) science team, was part of the NASA Southeast United States-based Studies of Emissions and Atmospheric Composition, Clouds and Climate Coupling by Regional Surveys (SEAC^{4}RS) mission, and collinear with a portion of the Southeast Atmosphere Study (SAS). This sensitive HSRL system provided first ever diurnal monitoring of well-calibrated aerosol backscatter in the

Southeast United States (SEUS) aerosol regime and provided an excellent narrative on summertime SEUS aerosol dynamics. The UW-HSRL deployment to Huntsville was an anchor point of the ground network of the SEAC^{4}RS campaign. We gave a detailed description of the system as well as other coincident ground-, airborne- and space-based data collections. Notably, the UAH lidar facility also hosted an Aerosol Robotic Network (AERONET) sun photometer and, during the early August late September SEAC^{4}RS campaign, near daily afternoon ozonesonde releases were made as part of the Southeast American Consortium for Intensive Ozonesonde Network Study (SEACIONS). A nearby Chemical Speciation Network (CSN) measurement station also provided surface particulate matter data. The Huntsville site was within 15 km of a CALIPSO orbit crossover point and in the middle of MISR orbit paths.

This paper provides the foundation for numerous ongoing studies utilizing the data sets described herein. Here we demonstrated the systems utility and identified canonical aerosol features and modes of variability commonly observed during the deployment. It is hoped that this analysis will provide some phenomenological context to the challenge of monitoring air quality or cloud condensation nuclei from space. A static 55 sr lidar ratio reconstructed overall AOT well, and a principle component analysis (PCA) was performed to identify covarying aerosol layers. Vertical correlations of factors were on the order of 1750 m for PBL factors, reducing to 200–900 m aloft for factors associated with individual layers or events. These factors guided the overall height binning for the analysis. Using an example day of 27 August 2013, a narrative is provided as to the nature of the UW-HSRL data to demonstrate typical boundary layer and free tropospheric pollution and biomass burning features. This information, coupled with AOT, surface particulate matter, and trajectory analyses, is then used to generate a deployment time series of aerosol and boundary layer features. Finally, three examples of aerosol phenomena are given that represent key aspects of the SEUS aerosol environment: (1) convective regimes, (2) frontal regimes, and (3) long range transport of biomass burning smoke. Key findings include the following:

1. Huntsville was in the middle of the SEUS haze belt with relatively flat topography and thus was likely representative in overall aerosol structure for the region. Average summertime 532 nm AOTs from AERONET at the site were on the order of ~0.2, with peaks as high as 0.55, and troughs as low as 0.025. Mean aerosol backscatter profiles were as expected based on other numerous airborne reports in the region: increasing to the top of the mixed layer (~1.2 km agl/1.4 km msl), with a decay to the middle troposphere. On average ~50% of total AOT can be attributed to the mixed layer taken as 1.2 km agl by the PCA analysis. Based on trajectory analyses and regional AOT maps, the surface was likely largely dominated by local anthropogenic/biogenic haze although local agricultural burning contributions are also likely. Backscatter and $PM_{2.5}$ in the 2013 summertime mixed layer peaked in August and September during the SEAC^{4}RS campaign. In the free troposphere, biomass burning plumes from an intense 2013 burning season were frequently observed throughout the study period, with the most significant event occurring in late June, but with the highest frequency in August.
2. When taken as an average, aerosol backscatter peaks at the top of the mixed layer and decays from the top of the mixed layer into the free troposphere. However, complex dynamics of the PBLs' mixed layer and entrainment zone were clearly evident in the data set. Clear air columns, presumably drier downdrafts, are also visible in between clouds extending from clouds through much of the mixed layer. While such features are commonly observed in the literature, the UW-HSRL data, to the best of our knowledge, provide the best precision to date of such complex structure with sensitivity to very tenuous aerosols features having backscatter cross sections smaller than the background molecular scattering. The PCA analysis suggests PBL's typical entrainment zone accounted for an additional ~25% of the overall AOT (that is, ~75% of total variance is explained by typical PBL heights). While clouds are often thought of as having "halos," UW-HSRL observations demonstrate that cloud outflow in the entrainment zone is in the form of spatially correlated detrainment layers. Indeed, observable downdrafts between fair weather clouds demonstrate that if such halos exist, they are very close to the cloud boundary. Finally, during fair weather periods the top of entrainment zone (and presumably the PBL) was capped by regional large-scale subsidence (often ~2.4–3 km msl/2.2–2.8 km agl). During convectively active regimes the 0°C level (~4.8–5.2 km msl altitude), the location of well-known increased stability, acts as a cap for warm fair weather boundary layer clouds.
3. Even in the presence of large-scale subsidence and shallow entrainment zones, the 0°C level also commonly delineated aerosol layering phenomena between the upper and lower free troposphere. "Warm"

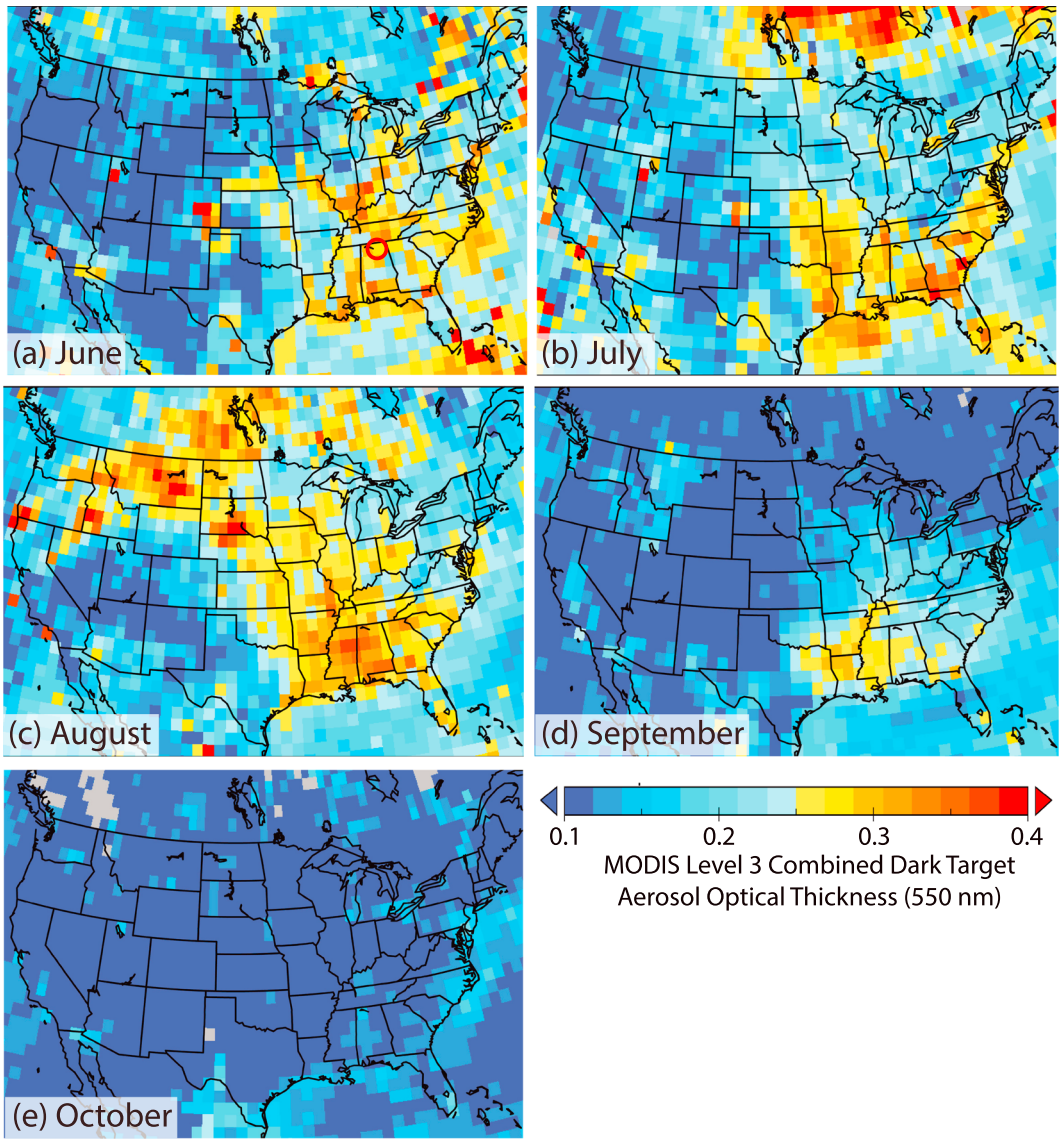

Figure A1. Monthly average MODIS AOT form the combined dark target level 3 product.

free tropospheric layers below this level were populated by long range smoke transport and plumes of deposited aerosol particles and moisture by clouds, accounting for 5–15% of AOT. Often multiple cloud and aerosol layers were present. Warm altocumulus with associated aerosol layers were also frequently observed at the top of the PBL and within the warm free troposphere, which leads to questions of possible aerosol cloud relationships in this important cloud genus. Above 0°C, smoke layers from the Pacific Northwest were observed. In several cases, dense plumes were observed in the upper free troposphere (above 0°C) to the base of the tropopause at ~13 km, accounting for the remaining ~10–15% of AOT variance. In the case study shown (22–24 June) smoke from a Colorado fire intersected with a Midwest mesoscale convective system (MCS) resulting in particularly strong injection to as high as 13 km. Some of the outflow of this event was so attenuating it was flagged as cirrus cloud in version 3.3 CALIPSO retrievals. The preliminary results from this data set suggest that topmost troposphere injections of smoke by MCSs may be a relative common occurrence during periods of significant fire emissions.

4. The diurnal monitoring of the aerosol backscatter profile combined with $PM_{2.5}$ data from the nearby CSN monitoring station provides significant insight into AOT-$PM_{2.5}$ relationships in fair weather,

convective, and frontal regimes alike. Examples provided give very clear demonstrations of how PBL surface layer aerosol properties are often decoupled from column AOT and provide perspective on trying to separate aerosol and humidity effects in entrainment zones and convective regimes [e.g., *Jeong and Li*, 2010; *Liu et al.*, 2011; *Ford and Heald*, 2013]. Indeed, our findings are consistent with the CALIPSO-based study of *Toth et al.* [2014] that even correlations between lidar attenuated backscatter as low as 400 m agl with $PM_{2.5}$ measurement at best have an r^2 value of 0.6. For example, during frontal passage, layer AOT fractions aloft can be substantially diminished. Postfrontal passage, AOT can remain low, but surface layer $PM_{2.5}$ recovers much more quickly. During convective events, there is clear evidence of pumping of mixed layer air into the free troposphere in deep and irregular entrainment zones, further reducing correlations.

Appendix A: Supplemental Figures to Support the Analysis

This appendix provides supplemental figures to provide context to the UW-HSRL deployment to the Huntsville, AL, site. Figure A1 provides monthly average MODIS Collection 6 combined dark target 550 nm AOT fields for June through October 2013—those months in which the lidar was in operation. By June 2013, AOT levels (and presumably particulate air pollution) were moderately high throughout the eastern United States. Summertime AOTs in 2013 peaked August through a combination of regional pollution and significant wildfire emissions from the Pacific Northwest. Indeed, a clear arc of high AOT is seen forming in Idaho and Montana through the Midwest and into the southeastern United States. Monthly average 550 nm AOTs in some locations surpassed 0.4. By September, fire activity diminished, except for agricultural burning in the Mississippi Valley. By late September and into October, the summer haze season had completed and average 550 nm AOTs throughout the United States dropped to < 0.15.

Back trajectories were completed for the entire UW-HSRL deployment to relate Huntsville lidar observations to regional AOT patterns. These are provided in Figure A2. Trajectories were spawned every 12 h from Huntsville to 3 days at five levels: 1 km msl (or 800 m agl) to represent boundary layer flow, 3 km to represent lower free troposphere, 4.5 km corresponding to the midtroposphere and mean 0°C melting level, 7 km for the upper troposphere, and 10 km, just beneath the tropopause. At the lowest altitudes, the Huntsville site was influenced from nearly everywhere in the eastern United States. At higher free troposphere levels, trajectories were progressively more associated with climatologically normal westerly winds. The one exception for this was mid-July where a week of strongly easterly winds existed over the site.

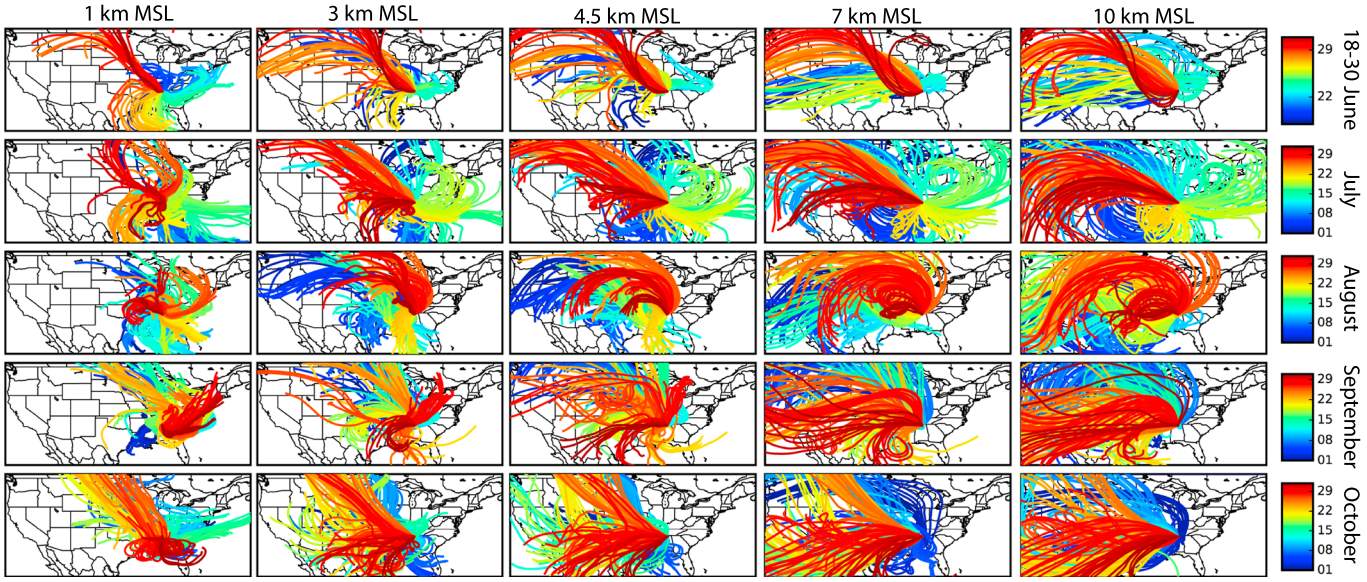

Figure A2. HYSPLIT back trajectories were spawned every 12 h over the Huntsville lidar site.

Acknowledgments
We are grateful to the senior leadership, management and scientists of the SEAC^{4}RS campaign, including campaign lead Owen B. Toon of the University of Colorado Boulder. Like all large field missions, the SEAC^{4}RS mission could not have occurred without the generous aid of regional scientists and engineers. We are grateful to the University of Alabama Regional Atmospheric Profiling Center for Discovery for the willingness to host and maintain the lidar as well as aid in the releasing of Southeast American Consortium for Intensive Ozonesonde Network Study ozonesondes. We also wish to thank the staff of the National Space Sciences Technology Center for other ancillary data set, which, were not all shown in this paper, nevertheless helped us in interpreting the lidar signal. Similarly, we are grateful to the staff supporting the CSN air quality network. Funding for the deployment of the UW-HSRL was provided by the CALIPSO science team as a contribution to the SEAC^{4}RS program. Analysis of the data presented here was provided by a NASA Atmospheric Composition Campaign Data Analysis and Modeling program (NNH14AY68I) and the Office of Naval Research Code 322 (N0001414AF00002). The SEAClONS network, organized at NASA/Goddard, was initially supported through a Grant to Penn State (NNX12AF05G). IMPROVE is a collaborative association of state, tribal, and federal agencies and international partners. The U.S. Environmental Protection Agency is the primary funding source, with contracting and research support from the National Park Service. The Air Quality Group at the University of California, Davis, is the central analytical laboratory, with ion analysis provided by the Research Triangle Institute and carbon analysis provided by the Desert Research Institute. IMPROVE data are available for download (http://vista.cira.colostate.edu/improve and http://views.cira.colostate.edu/fed). Lidar data presented here are available online at http://lidar.ssec.wisc.edu/. Data access was last verified for these sites on 14 January 2017. Finally, we are grateful for many helpful comments from three anonymous reviewers.

References

Angevine, W. M., H. K. Baltink, and F. C. Bosveld (2001), Observation of the morning transition of the convective boundary layer, *Boundary Layer Meteorol.*, *101*, 209–227, doi:10.1023/A:1019264716195.

Ansmann, A., M. Tesche, P. Seifert, D. Althausen, R. Engelmann, J. Fruntke, U. Wandinger, I. Mattis, and D. Müller (2009), Evolution of the ice phase in tropical altocumulus: SAMUM lidar observations over Cape Verde, *J. Geophys. Res.*, *114*, D17208, doi:10.1029/2008JD011659.

Arya, S. P. (1988), *Introduction to Micrometeorology*, Academic Press, San Diego, Calif.

Berg, L. K., L. K. Berg, J. A. Ogren, C. A. Hostetler, R. Ferrare, J. W. Hair, and J. M. Hubbe (2009), Overview of the cumulus humilis aerosol processing study, *Bull. Am. Meteorol. Soc.*, *90*, 1653, doi:10.1175/2009BAMS2760.1.

Boers, R., and E. W. Eloranta (1985), Lidar measurements of the atmospheric entrainment zone and the potential temperature jump across the mixed layer, *Boundary Layer Meteorol.*, *34*, 357–375.

Boers, R., E. W. Eloranta, and R. L. Coulter (1984), Lidar observations of mixed layer dynamics: Tests of parameterized entrainment models of mixed layer growth rate, *J. Climate Appl. Meteorol.*, *23*, 247–266, doi:10.1175/1520-0450(1984)023<0247:LOOMLD>2.0.CO;2.

Brooks, I. M. (2003), Finding boundary layer top: Application of a wavelet covariance transform to lidar backscatter profiles, *J. Atmos. Oceanic Technol.*, *20*, 1092–1105, doi:10.1175/1520-0426(2003)020<1092:FBLTAO>2.0.CO;2.

Burton, S. P., R. A. Ferrare, C. A. Hostetler, J. W. Hair, R. R. Rogers, M. D. Obland, C. F. Butler, A. L. Cook, D. B. Harper, and K. D. Froyd (2012), Aerosol classification using airborne high spectral resolution lidar measurements—Methodology and examples, *Atmos. Meas. Tech.*, *5*, 73–98, doi:10.5194/amt-5-73-2012.

Burton, S. P., M. A. Vaughan, R. A. Ferrare, and C. A. Hostetler (2014), Separating mixtures of aerosol types in airborne high spectral resolution lidar data, *Atmos. Meas. Tech.*, *7*, 419–436, doi:10.5194/amt-7-419-2014.

Campbell, J. R., D. L. Hlavka, E. J. Welton, C. J. Flynn, D. D. Turner, J. D. Spinhirne, V. S. Scott, and I. H. Hwang (2002), Full-time, eye-safe cloud and aerosol lidar observation at Atmospheric Radiation Measurement Program sites: Instrument and data processing, *J. Atmos. Oceanic Technol.*, *19*, 431e442.

Chalbot, M.-C., B. McElroy, and I. G. Kavouras (2013), Sources, trends and regional impacts of fine particulate matter in southern Mississippi valley: Significance of emissions from sources in the Gulf of Mexico coast, *Atmos. Chem. Phys.*, *13*, 3721–3732, doi:10.5194/acp-13-3721-2013.

Chew, B. N., J. R. Campbell, J. S. Reid, D. M. Giles, E. J. Welton, S. V. Salinas, and S. C. Liew (2011), Tropical cirrus cloud contamination in sun photometer data, *Atmos. Environ.*, *45*, 6724–6731, doi:10.1016/j.atmosenv.2011.08.017.

Chew, B. N., J. R. Campbell, S. V. Salinas, C. W. Chang, J. S. Reid, E. J. Welton, B. N. Holben, and S. C. Liew (2013), Aerosol particle vertical distributions and optical properties over Singapore, *Atmos. Environ.*, *79*, 599–613.

Chou, C. C. K., C. T. Lee, W. N. Chen, S. Y. Chang, T. K. Chen, C. Y. Lin, and J. P. Chen (2007), Lidar observations of the diurnal variations in the depth of the urban mixing layer: A case study on air quality deterioration in Taipei, Taiwan, *Sci. Total Environ.*, *374*, 156–166, doi:10.1016/j.scitotenv.2006.11.049.

Chu, D. A., et al. (2015), Regional characteristics of the relationship between columnar AOD and surface $PM_{2.5}$: Application of lidar aerosol extinction profiles over Baltimore-Washington Corridor during DISCOVER-AQ, *Atmos. Environ.*, *101*, 338–349.

Clarke, A., and V. Kapustin (2010), Hemispheric aerosol vertical profiles: Anthropogenic impacts on optical depth and cloud nuclei, *Science*, *329*, 1488–1492.

Clarke, A., et al. (2007), Biomass burning and pollution aerosol over North America: Organic components and their influence on spectral optical properties and humidification response, *J. Geophys. Res.*, *112*, D12S18, doi:10.1029/2006JD007777.

Cohn, S. A., and W. M. Angevine (2000), Boundary layer height and entrainment zone thickness measured by lidars and wind-profiling radars, *J. Appl. Meteorol.*, *39*, 1233–1247, doi:10.1175/1520-0450(2000)039<1233:BLHAEZ>2.0.CO;2.

Deshler, T., et al. (2008), Balloon experiment to test ECC-ozonesondes from different manufacturers, and with different cathode solution strengths: Results of the BESOS flight, *J. Geophys. Res.*, *113*, D04307, doi:10.1029/2007JD008975.

Draxler, R. R. (2004), HYSPLIT4 users' guide, last accessed March 2012. [Available at http://purl.access.gpo.gov/GPO/LPS47020.]

Draxler, R. R., and G. D. Hess (1997), Description of the HYSPLIT_4 modeling system, NOAA Tech. Memo. ERL ARL-224, 24 pp., NOAA Air Resources Laboratory, Silver Spring, Md.

Draxler, R. R., and G. D. Hess (1998), An overview of the HYSPLIT_4 modeling system of trajectories, dispersion, and deposition, *Aust. Meteorol. Mag.*, *47*, 295–308.

Drury, E., D. J. Jacob, R. J. D. Spurr, J. Wang, Y. Shinozuka, B. E. Anderson, A. D. Clarke, J. Dibb, C. McNaughton, and R. Weber (2010), Synthesis of satellite (MODIS), aircraft (ICARTT), and surface (IMPROVE, EPA-AQS, AERONET) aerosol observations over eastern North America to improve MODIS aerosol retrievals and constrain surface aerosol concentrations and sources, *J. Geophys. Res.*, *115*, D14204, doi:10.1029/2009JD012629.

Eck, T. F., et al. (2014), Observations of rapid aerosol optical depth enhancements in the vicinity of polluted cumulus clouds, *Atmos. Chem. Phys.*, *14*, 11,633–11,656, doi:10.5194/acp-14-11633-2014.

Eloranta, E. W. (2005), High spectral resolution lidar, in *Lidar: Range-Resolved Optical Remote Sensing of the Atmosphere*, edited by K. Weitkamp, Springer, New York.

Ferrare, R. A., D. D. Turner, L. H. Brasseur, W. F. Feltz, O. Dubovik, and T. P. Tooman (2001), Raman lidar measurements of the aerosol extinction-to-backscatter ratio over the Southern Great Plains, *J. Geophys. Res.*, *106*(D17), 20,333–20,347, doi:10.1029/2000JD000144.

Fochesatto, G. L., P. Drobinshi, C. Flamant, D. Guedalia, C. Sarrat, P. H. Flamant, and J. Pelon (2001), Evidence of the dynamical coupling between the residual layer and the developing convective boundary layer, *Boundary Layer Meteorol.*, *99*, 451–464, doi:10.1023/A:1018935129006.

Ford, B., and C. L. Heald (2013), Aerosol loading in the southeastern United States: Reconciling surface and satellite observations, *Atmos. Chem. Phys.*, *13*, 9269–9283, doi:10.5194/acp-13-9269-2013.

Fromm, M. D., and R. Servranckx (2003), Transport of forest fire smoke above the tropopause by supercell convection, *Geophys. Res. Lett.*, *30*(10), 1542, doi:10.1029/2002GL016820.

Fromm, M., D. T. Lindsey, R. Servranckx, G. Yue, T. Trickl, R. Sica, P. Doucet, and S. Godin-Beekmann (2010), The untold story of pyrocumulonimbus, *Bull. Am. Meteorol. Soc.*, *91*, 1193–1209, doi:10.1175/2010BAMS3004.1.

Fueglistaler, S., A. E. Dessler, T. J. Dunkerton, I. Folkins, Q. Fu, and P. W. Mote (2009), Tropical tropopause layer, *Rev. Geophys.*, *47*, RG1004, doi:10.1029/2008RG000267.

Garay, M. J., S. P. de Szoeke, and C. M. Moroney (2008), Comparison of marine stratocumulus cloud top heights in the southeastern Pacific retrieved from satellites with coincident ship-based observations, *J. Geophys. Res.*, *113*, D18204, doi:10.1029/2008JD009975.

Garrett, T. J., A. J. Heymsfield, M. J. McGill, B. A. Ridley, D. G. Baumgardner, T. P. Bui, and C. R. Webster (2004), Convective generation of cirrus near the tropopause, *J. Geophys. Res.*, *109*, D21203, doi:10.1029/2004JD004952.

Gedzelman, S. D. (1988), In praise of altocumulus, *Weatherwise*, *41*, 143–149, doi:10.1080/00431672.1988.9930533.
Guan, H., R. Esswein, J. Lopez, R. Bergstrom, A. Warnock, M. Follette-Cook, M. Fromm, and L. T. Iraci (2010), A multi-decadal history of biomass burning plume heights identified using aerosol index measurements, *Atmos. Chem. Phys.*, *10*, 6461–6469, doi:10.5194/acp-10-6461-2010.
Guiot, B., J. C. Roger, H. Cachier, P. C. Wang, J. H. Bai, and Y. Tong (2006), Impact of vertical atmospheric structure on Beijing aerosol distribution, *Atmos. Environ.*, *40*, 5167–5180, doi:10.1016/j.atmosenv.2006.03.051.
Hair, J. W., C. A. Hostetler, A. L. Cook, D. B. Harper, R. A. Ferrare, T. L. Mack, W. Welch, L. R. Izquierdo, and F. E. Hovis (2008), Airborne high spectral resolution lidar for profiling aerosol optical properties, *Appl. Opt.*, *47*, 6734–6752, doi:10.1364/AO.47.006734.
Hand, J. L., B. A. Schichtel, M. Pitchford, W. C. Malm, and N. H. Frank (2012), Seasonal composition of remote and urban fine particulate matter in the United States, *J. Geophys. Res.*, *117*, D05209, doi:10.1029/2011JD017122.
Hand, J. L., B. A. Schichtel, W. C. Malm, S. Copeland, J. V. Molenar, N. Frank, and M. Pitchford (2014), Widespread reductions in haze across the United States from the early 1990s through 2011, *Atmos. Environ.*, *94*, 671–679, doi:10.1016/j.atmosenv.2014.05.062.
Henne, S., M. Furger, S. Nyeki, M. Steinbacher, B. Neininger, S. F. J. de Wekker, J. Dommen, N. Spichtinger, A. Stohl, and A. S. H. Prévôt (2004), Quantification of topographic venting of boundary layer air to the free troposphere, *Atmos. Chem. Phys.*, *4*, 497–509, doi:10.5194/acp-4-497-2004.
Heymsfield, A. J. (1993), Microphysical structure of stratiform and cirrus clouds, in *Aerosol-Cloud-Climate Interaction*, edited by P. V. Hobbs, pp. 97–119, Academic Press, San Diego, Calif.
Hidy, G. M., C. L. Blanchard, K. Baumann, E. Edgerton, S. Tanenbaum, S. Shaw, E. Knipping, I. Tombach, J. Jansen, and J. Walters (2014), Chemical climatology of the southeastern United States, 1999–2013, *Atmos. Chem. Phys.*, *14*, 11,893–11,914, doi:10.5194/acp-14-11893-2014.
Holben, B. N., et al. (1998), AERONET—A federated instrument network and data archive for aerosol characterization, *Remote Sens. Environ.*, *66*, 1–16, doi:10.1016/S0034-4257(98)00031-5.
Jaffe, D. A., and N. L. Wigder (2012), Ozone production from wildfires: A critical review, *Atmos. Environ.*, *51*, 1–10.
Jeong, M.-J., and Z. Li (2010), Separating real and apparent effects of cloud, humidity, and dynamics on aerosol optical thickness near cloud edges, *J. Geophys. Res.*, *115*, D00K32, doi:10.1029/2009JD013547.
Jiménez-Escalona, J. C., and O. Peralta (2010), Processing of aerosol particles in convective cumulus clouds: Cases study in the Mexican East Pacific, *Adv. Atmos. Sci.*, *27*, 1331–1343, doi:10.1007/s00376-010-9114-3.
Johnson, R. H., P. E. Ciesielski, and K. A. Hart (1996), Tropical inversions near the 0°C level, *J. Atmos. Sci.*, *53*, 1838–1855.
Johnson, R. H., T. M. Rickenbach, S. A. Rutledge, P. E. Ciesiekski, and W. H. Schubert (1999), Trimodal characteristics of tropical convection, *J. Clim.*, *12*, 2397–2418.
Kahn, R. A., B. J. Gaitley, J. V. Martonchik, D. J. Diner, K. A. Crean, and B. Holben (2005), Multiangle Imaging Spectroradiometer (MISR) global aerosol optical depth validation based on 2 years of coincident Aerosol Robotic Network (AERONET) observations, *J. Geophys. Res.*, *110*, D10S04, doi:10.1029/2004JD004706.
Kaimal, J. C., J. C. Wyngaard, D. A. Haugen, O. R. Coté, Y. Izumi, S. J. Caughey, and C. J. Readings (1976), Turbulence structure in the convective boundary layer, *J. Atmos. Sci.*, *33*, 2152–2169.
Kaku, K. C., J. S. Reid, N. T. O'Neill, P. K. Quinn, D. J. Coffman, and T. F. Eck (2014), Verification and application of the extended spectral deconvolution algorithm (SDA+) methodology to estimate aerosol fine and coarse mode extinction coefficients in the marine boundary layer, *Atmos. Meas. Tech.*, *7*, 3399–3412, doi:10.5194/amt-7-3399-2014.
Kassianov, E., M. Ovchinnikov, L. K. Berg, S. A. McFarlane, C. Flynn, R. Ferrare, C. Hostetler, and M. Alexandrov (2010), Retrieval of aerosol optical depth in vicinity of broken clouds from reflectance ratios: Case study, *Atmos. Meas. Tech.*, *3*, 1333–1349, doi:10.5194/amt-3-1333-2010.
Kim, P. S., et al. (2015), Sources, seasonality, and trends of southeast US aerosol: An integrated analysis of surface, aircraft, and satellite observations with the GEOS-Chem chemical transport model, *Atmos. Chem. Phys.*, *15*, 10,411–10,433, doi:10.5194/acp-15-10411-2015.
Kleist, D. T., D. F. Parrish, J. C. Derber, R. Treadon, W. S. Wu, and S. Lord (2009), Introduction of the GSI into the NCEP Global Data Assimilation System, *Weather Forecasting*, *24*, 1691–1705, doi:10.1175/2009WAF2222201.1.
Kuang, S., J. F. Burns, M. J. Newchurch, S. Johnson, and S. Long (2011), Differential Absorption lidar to measure sub-hourly variation of tropospheric ozone profiles, *IEEE Trans. Geosci. Remote Sens.*, *49*, 557–571.
Kunkel, K. E., E. W. Eloranta, and S. T. Shipley (1977), Lidar observations of the convective boundary layer, *J. Appl. Meteorol.*, *16*, 1306–1311, doi:10.1175/1520-0450(1977)016<1306:LOOTCB>2.0.CO;2.
Levy, R. C., S. Mattoo, L. A. Munchak, L. A. Remer, A. M. Sayer, F. Patadia, and N. C. Hsu (2013), The Collection 6 MODIS aerosol products over land and ocean, *Atmos. Meas. Tech.*, *6*, 2989–3034, doi:10.5194/amt-6-2989-2013.
Lin, H.-W., J. L. McCarty, D. Wang, B. M. Rogers, D. C. Morton, G. J. Collatz, Y. Jin, and J. T. Randerson (2014), Management and climate contributions to satellite-derived active fire trends in the contiguous United States, *J. Geophys. Res. Biogeosci.*, *119*, 645–660, doi:10.1002/2013JG002382.
Liu, Y., Z. Wang, J. Wang, R. A. Ferrare, R. K. Newsom, and E. J. Welton (2011), The effect of aerosol vertical profiles on satellite-estimated surface particle sulfate concentrations, *Remote Sens. Environ.*, *115*, 508–513.
Liu, Z., M. A. Vaughan, D. M. Winker, C. A. Hostetler, L. R. Poole, D. Hlavka, W. Hart, and M. McGill (2004), Use of probability distribution functions for discriminating between cloud and aerosol in lidar backscatter data, *J. Geophys. Res.*, *109*, D15202, doi:10.1029/2004JD004732.
Lu, M.-L., J. Wang, R. C. Flagan, J. H. Seinfeld, A. Freedman, R. A. McClatchey, and H. H. Jonsson (2003), Analysis of humidity halos around trade wind cumulus clouds, *J. Atmos. Sci.*, *60*, 1041–1059.
Lynch, P., et al. (2016), An 11-year global gridded aerosol optical thickness reanalysis (v1.0) for atmospheric and climate sciences, *Geosci. Model Dev.*, *9*, 1489–1522, doi:10.5194/gmd-9-1489-2016.
Marchand, R., T. Ackerman, M. Smyth, and W. B. Rossow (2010), A review of cloud top height and optical depth histograms from MISR, ISCCP, and MODIS, *J. Geophys. Res.*, *115*, D16206, doi:10.1029/2009JD013422.
Markowicz, K. M., et al. (2016), Study of aerosol optical properties during long-range transport of biomass burning from Canada to central Europe in July 2013, *J. Aerosol Sci.*, *101*, 156–173, doi:10.1016/j.jaerosci.2016.08.006.
McCarty, J. L. (2011), Remote sensing estimates of annual and seasonal emissions from crop residue burning in the contiguous United States, *J. Air Waste Manage. Assoc.*, *61*, 22–34.
McGill, M., D. Hlavka, W. Hart, V. S. Scott, J. Spinhirne, and B. Schmidt (2002), Cloud physics lidar: Instrument description and initial measurement results, *Appl. Apt.*, *41*, 3725–3734, doi:10.1364/AO.41.003725.
Minnis, P., L. Nguyen, D. R. Doelling, D. F. Young, W. F. Miller, and D. P. Kratz (2002), Rapid calibration of operational and research meteorological satellite imagers, Part I: Evaluation of research satellite visible channels as references, *J. Atmos. Oceanic Technol.*, *19*, 1233–1249.
Minnis, P., et al. (2008a), Cloud detection in non-polar regions for CERES using TRMM VIRS and Terra and Aqua MODIS data, *IEEE Trans. Geosci. Remote Sens.*, *46*, 3857–3884.

Minnis, P., et al. (2008b), Near-real time cloud retrievals from operational and research meteorological satellites, *Proc. SPIE 7107, Remote Sensing of Clouds and the Atmosphere XIII, 7107-2*, 8 pp., Cardiff, Wales, U. K., 15–18 Sept.

Minnis, P., et al. (2011), CERES Edition-2 cloud property retrievals using TRMM VIRS and Terra and Aqua MODIS data, Part I: Algorithms, *IEEE Trans. Geosci. Remote Sens.*, *49*(11), 4374–4400.

Müller, D., A. Ansmann, I. Mattis, M. Tesche, U. Wandinger, D. Althausen, and G. Pisani (2007), Aerosol-type-dependent lidar ratios observed with Raman lidar, *J. Geophys. Res.*, *112*, D16202, doi:10.1029/2006JD008292.

Newchurch, M. J., M. A. Ayoub, S. Oltmans, B. Johnson, and F. J. Schmidlin (2003), Vertical distribution of ozone at four sites in the United States, *J. Geophys. Res.*, *108*(D1), 4031, doi:10.1029/2002JD002059.

O'Neill, N. T., T. F. Eck, A. Smirnov, B. N. Holben, and S. Thulasiraman (2003), Spectral discrimination of coarse and fine mode optical depth, *J. Geophys. Res.*, *108*(D17), 4559, doi:10.1029/2002JD002975.

Ott, L. E., et al. (2016), Frequency and impact of summertime stratospheric intrusions over Maryland during DISCOVER-AQ (2011): New evidence from NASA's GEOS-5 simulations, *J. Geophys. Res. Atmos.*, *121*, 3687–3706, doi:10.1002/2015JD024052.

Pal, S., T. R. Lee, S. Phelps, and S. F. J. De Wekker (2014), Impact of atmospheric boundary layer depth variability and wind reversal on the diurnal variability of aerosol concentration at a valley site, *Sci. Total Environ.*, *496*, 424–434, doi:10.1016/j.scitotenv.2014.07.067.

Parungo, F., J. F. Boatman, S. W. Wilkison, H. Sievering, and B. B. Hicks (1994), Trends in global marine cloudiness and anthropogenic sulfur, *J. Clim.*, *7*, 434–440, doi:10.1175/1520-0442(1994)007<0434:TIGMCA>2.0.CO;2.

Peterson, D. A., E. J. Hyer, J. R. Campbell, M. D. Fromm, J. W. Hair, C. F. Butler, and M. A. Fenn (2015), The 2013 Rim Fire: Implications for predicting extreme fire spread, pyroconvection, and smoke emissions, *Bull. Am. Meteorol. Soc.*, *96*, 229–247, doi:10.1175/BAMS-D-14-00060.1.

Piironen, A., and E. W. Eloranta (1995), Convective boundary layer mean depths, cloud base altitudes, cloud top altitudes, cloud coverages, and cloud shadows obtained from volume imaging lidar data, *J. Geophys. Res.*, *100*(D12), 25,569–25,576, doi:10.1029/94JD02604.

Platnick, S., M. D. King, S. A. Ackerman, W. P. Menzel, B. A. Baum, J. C. Riedi, and R. A. Frey (2003), The MODIS cloud products: Algorithms and examples from Terra, *IEEE Trans. Geosci. Remote Sens.*, *41*, 459–473, doi:10.1109/TGRS.2002.808301.

Platnick, S., et al. (2016), The MODIS cloud optical and microphysical products: Collection 6 updates and examples from Terra and Aqua, *IEEE Trans. Geosci. Remote Sens.*, *55*, 502–525, doi:10.1109/TGRS.2016.2610522.

Posselt, D. J., S. C. van den Heever, and G. L. Stephens (2008), Trimodal cloudiness and tropical stable layers in simulations of radiative convective equilibrium, *Geophys. Res. Lett.*, *35*, L08802, doi:10.1029/2007GL033029.

Radke, L. F., and P. V. Hobbs (1991), Humidity and particle fields around some small cumulus clouds, *J. Atmos. Sci.*, *48*, 1190–1193, doi:10.1175/1520-0469(1991)048<1190:HAPFAS>2.0.CO;2.

Sassen, K., and V. I. Khvorostyanov (2008). Cloud effects from boreal forest fires smoke: Evidence for ice nucleation from polarization lidar data and cloud model simulations, *Environ. Res. Let.*, *3*, 025006 doi:10.1088/1748-9326/3/2/025006.

Sassen, K., and Z. Wang (2012), The clouds of the middle troposphere: Composition, radiative impact, and global distribution, *Surv. Geophys.*, *33*, 677–691, doi:10.1007/s10712-011-9163-x.

Sessions, W. R., et al. (2015), Development towards a global operational aerosol consensus: Basic climatological characteristics of the International Cooperative for Aerosol Prediction Multi-Model Ensemble (ICAP-MME), *Atmos. Chem. Phys.*, *15*, 335–362, doi:10.5194/acp-15-335-2015.

Shinozuka, Y., A. D. Clarke, S. G. Howell, V. N. Kapustin, C. S. McNaughton, J. Zhou, and B. E. Anderson (2007), Aircraft profiles of aerosol microphysics and optical properties over North America: Aerosol optical depth and its association with PM2.5 and water uptake, *J. Geophys. Res.*, *112*, D12S20, doi:10.1029/2006JD007918.

Shipley, S. T., D. H. Tracy, E. W. Eloranta, J. T. Trauger, J. T. Sroga, F. L. Roesler, and J. A. Weinman (1983), High spectral resolution lidar to measure optical scattering properties of atmospheric aerosols. 1: Theory and instrumentation, *Appl. Opt.*, *22*, 3716–3724.

Smirnov, A., B. N. Holben, T. F. Eck, O. Dubovik, and I. Slutsker (2000), Cloud screening and quality control algorithms for the AERONET data base, *Remote Sens. Environ.*, *73*, 337–349.

Smit, H. G. J., et al. (2007), Assessment of the performance of ECC-ozonesondes under quasi-flight conditions in the environmental simulation chamber: Insights from the Jülich Ozone Sonde Intercomparison Experiment (JOSIE), *J. Geophys. Res.*, *112*, D19306, doi:10.1029/2006JD007308.

Solomon, P. A., D. Crumpler, J. B. Flanagan, R. K. M. Jayanty, E. E. Rickman, and C. E. McDade (2014), US national $PM_{2.5}$ chemical speciation monitoring networks–CSN and IMPROVE: Description of networks, *J. Air Waste Manage. Assoc.*, *64*, 1410–1338, doi:10.1080/10962247.2014.956904.

Stauffer, R. M., G. A. Morris, A. M. Thompson, E. Joseph, G. J. R. Coetzee, and N. R. Nalli (2014), Propagation of radiosonde pressure sensor errors to ozonesonde measurements, *Atmos. Meas. Tech.*, *7*, 65–79, doi:10.5194/amt-7-65-2014.

Stull, R. B. (1988), *An Introduction to Boundary Layer Meteorology*, Atmospheric and Oceanographic Library, Kluwer Acad., Dordrecht, Netherlands.

Su, W., G. L. Schuster, N. G. Loeb, R. R. Rogers, R. A. Ferrare, C. A. Hostetler, J. W. Hair, and M. D. Obland (2008), Aerosol and cloud interaction observed from high spectral resolution lidar data, *J. Geophys. Res.*, *113*, D24202, doi:10.1029/2008JD010588.

Tackett, J. L., and L. Di Girolamo (2009), Enhanced aerosol backscatter adjacent to tropical trade wind clouds revealed by satellite-based lidar, *Geophys. Res. Lett.*, *36*, L14804, doi:10.1029/2009GL039264.

Thompson, A. M., et al. (2007), Intercontinental Chemical Transport Experiment Ozonesonde Network Study (IONS) 2004: 1. Summertime upper troposphere/lower stratosphere ozone over northeastern North America, *J. Geophys. Res.*, *112*, D12S12, doi:10.1029/2006JD007441.

Thornhill, K. L., et al. (2008), The impact of local sources and long-range transport on aerosol properties over the northeast U.S. region during INTEX-NA, *J. Geophys. Res.*, *113*, D08201, doi:10.1029/2007JD008666.

Toon, O. B., et al. (2016), Planning, implementation, and scientific goals of the Studies of Emissions and Atmospheric Composition, Clouds and Climate Coupling by Regional Surveys ($SEAC^4RS$) field mission, *J. Geophys. Res. Atmos.*, *121*, 4967–5009, doi:10.1002/2015JD024297.

Torres, O., A. Tanskanen, B. Veihelmann, C. Ahn, R. Braak, P. K. Bhartia, P. Veefkind, and P. Levelt (2007), Aerosols and surface UV products from Ozone Monitoring Instrument observations: An overview, *J. Geophys. Res.*, *112*, D24S47, doi:10.1029/2007JD008809.

Toth, T. D., J. Zhang, J. R. Campbell, E. J. Hyer, J. S. Reid, Y. Shi, and D. L. Westphal (2014), Impact of data quality and surface-to-column representativeness on the $PM_{2.5}$/satellite AOD relationship for the contiguous United States, *Atmos. Chem. Phys.*, *14*, 6049–6062, doi:10.5194/acp-14-6049-2014.

Twohy, C. H., J. A. Coakley, and W. R. Tahnk (2009), Effect of changes in relative humidity on aerosol scattering near clouds, *J. Geophys. Res.*, *114*, D05205, doi:10.1029/2008JD010991.

Uthe, E. E. (1972), Lidar observations of the urban aerosol structure, *Bull. Am. Meteorol. Soc.*, *53*, 358.

Val Martin, M., J. A. Logan, R. A. Kahn, F.-Y. Leung, D. L. Nelson, and D. J. Diner (2010), Smoke injection heights from fires in North America: Analysis of 5 years of satellite observations, *Atmos. Chem. Phys.*, *10*, 1491–1510, doi:10.5194/acp-10-1491-2010.

Wagner, N. L., et al. (2015), In situ vertical profiles of aerosol extinction, mass, and composition over the southeast United States during SENEX and SEAC^{4}RS: observations of a modest aerosol enhancement aloft, *Atmos. Chem. Phys.*, *15*, 7085–7102, doi:10.5194/acp-15-7085-2015.

Wang, J. and S. A. Christopher (2003), Intercomparison between satellite derived aerosol optical thickness and $PM_{2.5}$ mass: Implications for air quality studies, *Geophys. Res. Lett.*, *30*(21), 2095, doi:10.1029/2003GL018174.

Weber, R. J., et al. (2007), A study of secondary organic aerosol formation in the anthropogenic-influenced southeastern United States, *J. Geophys. Res.*, *112*, D13302, doi:10.1029/2007JD008408.

Winker, D. M., and C. R. Trepte (1998), Laminar cirrus observed near the tropical tropopause by LITE, *Geophys. Res. Lett.*, *25*, 3351–3354, doi:10.1029/98GL01292.

Winker, D. M., M. A. Vaughan, A. Omar, Y. X. Hu, K. A. Powell, Z. Y. Liu, W. H. Hunt, and S. A. Young (2008), Overview of the CALIPSO mission and CALIOP data processing algorithms, *J. Atmos. Oceanic Technol.*, *26*, 2310–2323, doi:10.1175/2009JTECHA1281.1.

Wonaschuetz, A., A. Sorooshian, B. Ervens, P. Y. Chuang, G. Feingold, S. M. Murphy, J. de Gouw, C. Warneke, and H. H. Jonsson (2012), Aerosol and gas re-distribution by shallow cumulus clouds: An investigation using airborne measurements, *J. Geophys. Res.*, *117*, D17202, doi:10.1029/2012JD018089.

Xu, L., et al. (2015), Effects of anthropogenic emissions on aerosol formation from isoprene and monoterpenes in the southeastern United States, *Proc. Natl. Acad. Sci. U.S.A.*, *112*, 37–42, doi:10.1073/pnas.1417609112.

Yu, P., et al. (2016), Surface dimming by the 2013 Rim Fire simulated by a sectional aerosol model, *J. Geophys. Res. Atmos.*, *121*, 7079–7087, doi:10.1002/2015JD024702.

Ziemba, L. D., et al. (2013), Airborne observations of aerosol extinction by in situ and remote-sensing techniques: Evaluation of particle hygroscopicity, *Geophys. Res. Lett.*, *40*, 417–422, doi:10.1029/2012GL054428.